LASER SURFACE MELTING OF CARBON COATED AA7075 ALUMINUM ALLOY: STRUCTURAL TRANSFORMATIONS AND TRIBOLOGICAL BEHAVIOR

By

SOURABH BISWAS

Bachelor of Engineering in Metallurgy and Materials Engineering

Bengal Engineering and Science University, Shibpur

Shibpur, West Bengal

2011

Submitted to the Faculty of the
Graduate College of the
Oklahoma State University
in partial fulfillment of
the requirements for
the Degree of
MASTER OF SCIENCE
July, 2014

LASER SURFACE MELTING OF CARBON COATED AA7075 ALUMINUM ALLOY: STRUCTURAL TRANSFORMATIONS AND TRIBOLOGICAL BEHAVIOR

Thesis Approved:

Dr. Sandip P. Harimkar

Thesis Adviser

Dr. A. Kaan Kalkan

Dr. Ranji Vaidyanathan

ACKNOWLEDGEMENTS

I would like to acknowledge the help and support of my adviser, Dr. Sandip P. Harimkar, for his valuable technical input and directions that enabled me to complete this project. His immense experience in research, in addition to his positive attitude and motivation for the last two years, has been the key to my accomplishment. I would also like to express my sincere gratitude to Dr. Kaan Kalkan for being in my thesis committee and also for allowing me to perform Raman Spectroscopy analysis for my research. I am really thankful for his valuable inputs on the results and his constant support. I am also highly grateful to Dr. Ranji Vaidyanathan for being in my thesis committee and for his useful discussions concerning my research. I am also thankful to the National Science Foundation (Grant No.: CMMI-1149079) for supporting this project.

I feel extremely proud and privileged to be part of the Multiscale Materials Processing and Characterization Group, as it gave me some of my best friends and colleagues. I am really grateful to S. Habib Alavi, Ashish Singh, Farhad, Redwan, Aditya and all others for being so helpful and supportive to me to achieve my goals. From performing experiments to giving insights to the results, they had been highly patient and helpful colleagues. I would also like to acknowledge my parents, Mr. Sanjoy Biswas and Mrs. Amita Biswas, as it was their enthusiasm and support which gave me strength at my darkest moments when I had lost all hope. I also want to express my gratitude for my sister, Saptami Biswas, my cousin Arnab Sinha, and my sister-in-law Shaoni Sinha for their unconditional love and care. I am thankful to my friends, Romit, Rehan, Kanishka, Sayan, Rohit, Madhura, and Subhashree to have made my life in Stillwater so nice and pleasant. I really enjoyed all the debates we did on almost every topic on earth that almost convinced me that I could be the president of any nation with such advisers.

Last but not the least; I would like to thank all my friends and well-wishers who have supported me in my life and I am dedicating this work to each and every one of them.

Name: SOURABH BISWAS

Date of Degree: JULY, 2014

Title of Study: LASER SURFACE MELTING OF CARBON COATED AA7075 ALUMINUM ALLOY: STRUCTURAL TRANSFORMATIONS AND TRIBOLOGICAL BEHAVIOR

Major Field: MECHANICAL AND AEROSPACE ENGINEERING

Abstract: Carbon is one of the most common solid lubricants and has often been used to achieve superior tribological properties. In this investigation, a CO_2 laser in continuous wave mode was used to develop diamond-like carbon (DLC)-rich coatings on 7075 alloys. A detailed investigation on the effect of the in-situ transformed DLC and graphitic nanoparticles on the tribological properties of the 7075 alloys was performed. A unique relationship between the surface hardness and wear rate was noted, wherein the wear rate decreased with decrease in surface hardness after the laser surface engineering. An analysis of wear track and counterbody using EDS and Raman spectroscopy confirmed the formation of metastable DLC-rich graphitic tribolayer during the wear process. A 'reverse' transformation of the apparently more stable graphitic carbon to metastable DLCs in the tribolayer during frictional loadings was also noticed. The tribolayer was noted to generate significant lubricating action, and therefore, improve the wear resistance. Also, unlike the loss in lubricating action with increasing time usually exhibited by non-hydrogenated DLCs, the increase in nano-carbon rich melt-zone was observed to partially mitigate this effect by enabling presence of lubricating particles even at greater depths from the surface.

TABLE OF CONTENTS

LIST OF TABLES

LIST OF FIGURES

CHAPTER I

INTRODUCTION

1.1 Development of carbon coating using laser surface engineering

Carbon has been historically often been used to improve frictional properties between contacting surfaces and has inspired several research endeavors. Hence, studies concerning the improvement in the tribological properties of materials post surface treatment using various allotropes of carbon like graphene [1, 2], multi-walled carbon nanotubes (MWCNTs) [3], diamond-like carbon (DLC) [4] has been reported. Each study mentioned a marked improvement in coefficient of friction and wear resistance as compared to the base received materials. Every mentioned allotrope of carbon has unique physical properties that make them highly effective lubricants. For example, while graphitic sp2 carbon is chemically stable as well as extremely lubricating [5], DLC has been reported to exhibit outstanding hardness as well as extremely low coefficient of friction[6]. Development of DLC coatings has been reported using several processing routes such as laser irradiation [7], plasma immersion ion processing [8], RF glow discharge, DC magnetron sputtering, ion beam generated from cathodic discharge with varying success [9].

It should be noted though, that embedment of carbon particles in the substrate surface can not only improve lubrication but also eliminate the bonding concerns of carbon with substrate. Now, extensive investigations on the tribological behavior of bulk processed of carbon based composites have been performed. For instance, tribological studies of bulk carbon based composites like Al-CNT [10], Cu-

Graphite [11], Ni-CNT composites [12] using novel processing routes like spark plasma sintering, powder metallurgy, and pulse electrodeposition respectively has been reported. However, surface alloying using carbon particle embedment has been, relatively unexplored. However, this approach appears highly promising, as the process of embedment of carbon particles enables the lubrication action for considerably longer periods of time, due to the notable presence of lubricating particles along much greater depths (the entire embedment zone). Laser irradiation often involves melting of the substrate's surface and thus can naturally generate the previous mentioned conditions of carbon embedment along thicker melt zones in addition to transformation of precursor carbon to DLC. These features, therefore, renders laser irradiation a particular edge as a processing technique. Also, extremely high levels of control and precision have been reported to be achieved in laser processing [13]. Hence, apart from conventional applications, this feature makes laser processing the preferred processing route in developing extremely thin films as protective coatings [14].

The choice of processing route and substrate material has been reported to be significantly influence the nature of DLC developed. For example, the presence and amount of hydrogen in the DLC was reported to prolong the lubrication time in Donnet *et al* [15]. The reason is probably due to the reduction of interacting carbon with the wear ball as reported by the molecular dynamics simulations of Schall *et al* [16]. Also, the primary laser parameter employed in developing laser irradiated DLC-rich surfaces has been use of pulse mode and high frequency lasers [17-20]. The ease in photolytic splitting of C-C bonds due to highly localized irradiation area associated with pulse-laser irradiation can be considered as the primary reason for such high preference [21]. Also, since the extent of photolytic splitting of C-C bonds increases with increase in laser frequency, the use of higher frequency excimer ($\lambda \approx$ 126-351 nm) and to some extent Nd:YAG lasers (λ = 1.06 μm) can be explained. However, the comparatively higher powers achieved by the CO_2 lasers, can be harnessed to generate DLC from precursor carbon. Interestingly, the limited study of CO_2 laser induced DLC generation has primarily

targeted use of hydrocarbons such as C_2H_4 as precursor carbon source instead of elementary solid graphitic carbon [22].

Based on these investigations, generation of DLCs from elemental sp2 carbon using CO_2 laser in continuous mode was studied. Aluminum 7075 alloys as substrate material was used in the present investigation. The 7075 alloys are noted for their very high strength to weight ratio and this explains their high popularity as aircraft body materials. Also, their response to precipitation during heat treatment (due to presence of alloying elements like Zn, Mg, Cu) make the study of their phase evolution with time and temperature a very popular field of scientific investigation. However, since aircraft bodies are often subjected to moving contacting surfaces, and therefore, extensive investigation on the wear analysis on these alloys has been reported in dry ball-on-pin [23, 24] and fretting mechanisms [25, 26]. Laser surface engineering to improve wear resistance of these alloys has also been reported by Yue *et al* [27]. However, the philosophy concerning improved wear performance has primarily been incorporation of hard ceramic/intermetallic phases at the surface and not much work in the in-situ lubrication has been reported. Therefore, to understand the structure-property correlations during laser irradiation on the precipitation hardenable aluminum (PHA) alloys, a comparative study on the laser surface engineering of three major PHA alloys was performed.

1.2 Laser surface engineering of PHA alloys

1.2.1 Aluminum alloys

Aluminum (Al) is the third most abundant element and constitutes as high as 8% of the earth's crust, which is about 50% greater than the next most abundant metal, iron. Initially limited by the difficulties in reducing and extracting Al due to its abnormally high oxygen affinity, the immense cost of production and inherent silvery luster turned the value of Al comparable with that of gold in monetary

terms. Since the development of Hall-Heroult process and other innovations in extraction technologies, the cost of Al production has declined exponentially. From the first attempt in commercial production of Al in 1888 by Alcoa [28], Al alloys have progressed significantly in their rather young history.

A very low density (2.7 g/cm^3) gives Al excellent specific properties, and its face-centered cubic crystal structure inherently renders the alloys with marked hot forming ability. Also, Al alloys have appreciable castability and corrosion resistance. The selection of materials is becoming increasingly competitive in recent times, and consumers often select a material based on a number of properties, performance, and economic factors. The abundant availability and attractive properties have given Al a distinct edge over other engineering alloys. The popularity of Al can be inferred from the fact that within the first century of commercialized Al production, Al has replaced Cu to become the most produced non-ferrous metal [29, 30].

Although the cost of Al per unit mass has declined significantly in the past century, it is reported as one of the most popular materials used in research. This popularity can be attributed to its wide spectrum of applications and potential for developing desired properties with varying heat treatments and alloying additions. The wrought Al alloy systems successfully developed for commercial applications is presented in Table 1.1 [31].

Among the commercially developed wrought Al alloys, only 2xxx, 6xxx, and 7xxx (and still developing 8xxx) series alloys are heat treatable by precipitation hardening [32]. An important feature of the PHA alloy systems is the rapidly decreasing solid solubility with decreasing temperature. The sharply sloping solvus line increases the ease of formation of intermetallic phases such as Guiner-Preston (GP) zones in Al-Cu system upon age hardening. This feature offers an excellent control in developing a microstructure with desired mechanical properties, rendering these systems a distinct edge over other commercial alloy systems such as Fe-based systems [33, 34].

Table 1.1 Principle alloying elements in wrought Al alloys [31]

Alloy Series	Principal Alloying Element
1xxx	None
2xxx	Cu
3xxx	Mn
4xxx	Si
5xxx	Mg
6xxx	Mg and Si
7xxx	Zn
8xxx	Miscellaneous

Among all the Al alloys, the PHA alloys offer the highest specific strength, one of the most critical parameters for material selection in aerospace, automobile, defense, structural, and sport applications. Also, as fuel economy is becoming increasingly important due to the acute shortage of fossil fuels, reducing weight of vehicles to improve fuel efficiency is gaining more importance. This again underlines the importance of PHA alloys in these applications. Apart from the unmatched strength of the PHA alloys, their non-heat treatable counterparts also trail in some attributes extremely essential in certain applications. For example, 5xxx series Al-Mg alloys exhibit dynamic strain ageing behavior [35], and hence, often suffers from inadequate surface finish after forming to meet the high standards for applications in automobile industry.

Al alloys offer excellent corrosion resistance owing to their high oxygen affinity. Al alloys form an extremely dense (non-porous) and conformal protective oxide layer, promoting their popularity in structural applications. However, the corrosion resistance of PHA alloy systems such as 2024 [36], 6061

[37, 38], and 7075 [39] is significantly affected by the presence of highly electropositive precipitates [40]. Although precipitation during age hardening is vital for improving the strength of Al alloys, it also tends to form internal corrosion cells with the base Al alloy matrix as the electronegativity of the matrix is almost always greater than the precipitates. Therefore, to achieve an optimum combination of both enhanced strength as well as corrosion resistance in the PHA alloys, several surface engineering based technologies have been developed. Brazing, anodizing, plasma electrolytic oxidation (PEO), chemical vapor deposition (CVD), and laser surface engineering (LSE) are some of the most successful approaches developed to achieve superior surface properties. While each of these processes have its advantages and limitations, LSE approaches are becoming increasingly important for improving the mechanical and electrochemical properties of PHA alloys. The improvement in surface properties of these alloys is essential to sustain extreme environments often experienced in components such as fuel exhaust nozzles, fuselage bodies, and aircraft structures. In this paper, various LSE approaches for surface modifications of three most common PHA alloys (2024, 6061, and 7075) are critically reviewed. An assessment of the reported data to understand the influence of laser processing parameters on the development of microstructure (grain refinement, compositional segregation, selective vaporization, *in-situ* reactions, and formation of intermetallic phases) and mechanical/electrochemical properties is also presented.

1.2.2 Laser Surface Engineering

Surface engineering generally involves modification of the microstructure and composition of the surfaces to improve the surface properties without significantly altering the base/substrate material properties. Lasers are becoming increasingly important in surface engineering of wide range of materials including metals, alloys, ceramics, composites, and polymers. The laser surface engineering approaches have been successfully used to improve hardness, strength, toughness, wear resistance, corrosion resistance, heat resistance, and fatigue resistance of materials. For example, the use of LSE approaches in preventing/minimizing corrosion has been successfully demonstrated in various alloy systems such as Al

[41], Ti [42], and Fe-based alloys [43]. Three major approaches for LSE of light alloys are laser surface melting (LSM), laser surface alloying (LSA), and laser composite surfacing (LCS). All of these approaches involve laser material interaction that causes surface melting of the alloy. In LSM, a laser is irradiated on the surface causing melting and rapid resolidification of the alloy. Very high cooling rates of the order of up 10^5-10^{11} K/s during resolidification results in the formation of refined dendritic microstructure in the surface. The properties improvement in LSM is primarily due to microstructural refinement and compositional redistribution in laser modified surface. In LSA, the composition of the surfaces is modified by introducing additional desired element during surface melting. The alloying of the surface can be accomplished either by feeding the elemental powder in melt pool or by preplacing the elemental powder on the substrate before laser surface melting. The compositional modification together with microstructural refinement at the surface leads to improvement in surface properties. LCS involves introducing hard phase particles in the laser melted pool forming metal matrix composite surface. The hard phase particles are fed into the melt pool or preplaced on the substrate before laser surface melting. LCS can also be accomplished by in-situ reactions in the laser melted surfaces. The composite structure and microstructural refinement results in combination of surface properties in LCS surfaces. Depending on the incident laser power, laser scanning velocity, and focus conditions and thermo-physical properties of the material, the depth of surface modification up to 1-2 mm can be readily achieved in a range of materials. LSE also offers distinct advantages such as non-contact processing, ease of automation, rapid processing, flexible manufacturing, and minimum heat affected zones, and ability to produce a range of microstructural/compositional effects.

All the LSE approaches such as LSM, LSA, and LCS have been successfully demonstrated for different Al alloys. Main objective of LSE for PHA alloys is to achieve optimum combination of corrosion resistance and hardness/wear resistance at the surface. LSM and LSA are particularly important for improving corrosion resistance of relatively stronger PHA alloys such as 2024 and 7075 alloys. For

corrosion resistant 6061 PHA alloys, LCS processes have been extensively used to improve surface hardness and wear resistance. Various effects such as microstructure refinement (dendritic microstructure), compositional segregation (copper enrichment at the grain boundaries), compositional modifications (through selective vaporization and surface alloying), and in-situ reactions (formation of intermetallic phases of aluminum) have been observed during LSE of PHA alloys.

1.2.3 AA2024 Alloys

The 2024 Al alloys, with Cu as its primary alloying element, are one of the most popular and earliest developed Al alloys. The chemical composition of this alloy is given in Table 1.2 [31].

The 2024 alloy is age hardenable, and distinct phases such as GP zone I, GP zone II, θ', and equilibrium θ have been identified to precipitate during the age hardening treatment depending both on the treatment temperature and time. Although this alloy exhibits comparatively higher tensile strength as observed from Table 1.3 [31], it is reported to be severely susceptible to pitting corrosion.

The corrosion behavior of 2024 alloys was investigated in detail by Liao *et al* [44]. The formation of microstructural galvanic couples in this alloy was studied by performing potentiodynamic corrosion tests in 0.5 M NaCl solution.

Table 1.2 Typical chemical compositions of common precipitation hardenable Al alloys [31]

Alloy	Ultimate Tensile Strength (MPa)
2024	475
6061	310
7075	572

Table 1.3 Typical ultimate tensile strengths of the 2024, 6061, and 7075 alloys at T6 temper condition [31]

Alloy	Composition (wt.%)						
	Si	Cu	Mn	Mg	Cr	Zn	Al
2024	..	4.5	0.6	1.5	..	..	Balance
6061	0.6	0.25	..	1.0	0.20	..	Balance
7075	..	1.6	..	2.5	0.30	5.6	Balance

The influence of the microstructural species was examined using SEM/optical microscopy and XRD techniques. The studies showed that corrosion in the 2024 alloy systems occurred primarily in two distinct stages. Initial pitting occurred only along the interfaces of highly electropositive precipitates with matrix and was not very severe, as observed in Fig. 1.1(a).

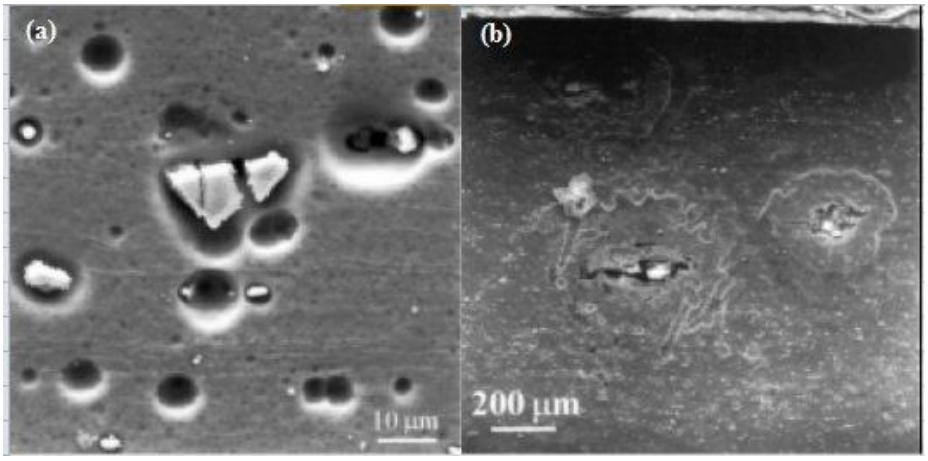

Fig. 1.1 (a) General pitting (first stage), and (b) severe pitting (second stage) in 2024 Al alloys [44]

However, the later stage of pitting, as shown in Fig. 1.1(b), commences when the passive Al oxide layer adhering to the surface is removed. The corrosion in the later stage was observed not only at the coarser precipitate-matrix interfaces but also at the interfaces of the matrix and the solute clusters,

even though such interfaces have noticeably lower corrosion potential. The dramatic rise in corrosion rate was attributed to the removal of corrosion resistant Al_2O_3 layer, and subsequent exposure of the matrix. Also, the solute clusters, most likely the GP zones, are more dispersed than equilibrium θ phases, increasing significantly the formation of a statistical probability of microstructural corrosion cell. This explains the susceptibility of 2024 Al alloys to corrosion in aggressive atmosphere often encountered by aircraft structures (moisture, acid rain, and environmental emissions). Intergranular corrosion is also an often reported issue with these alloy systems, as the grain boundaries act as preferential precipitation sites and hence increase chances of corrosion cell formation at the grain boundaries [45, 46]. Most of the efforts in LSE of these 2024 alloys are focused on achieving optimum combination of corrosion resistance and surface mechanical properties.

1.2.3.1 Laser Surface Melting of AA2024 Alloys

1.2.3.1.1 Corrosion Behavior

The refined dendritic surface microstructure with finer precipitates and compositional effects often generated by LSM treatments is particularly effective in improving corrosion resistance. The corrosion behavior of LSM treated AA2024-T351 was investigated by Li *et al* [47]. The LSM was conducted using a 2 kW CO_2 laser. The LSM treated microstructures revealed that the rapid solidification during high power LSM treatment not only reduces the grain size by formation of finer dendrites but also influences the precipitation chemistry. The resolidification of the surface initiates appreciable segregation of Cu to the grain boundaries due to constitutional supercooling. The higher Cu concentration at grain boundaries is virtually unaffected as diffusion of copper in Al matrix is very sluggish. The diffusion is further restricted as the temperature at the surface falls rapidly due to the high quenching rates associated with laser processing. The insufficient amount of Cu in the grain interior reduces the volume of θ phases which are very susceptible to corrosion. Also, as Cu segregation reduces grain boundary energy of the

alloy, the grain boundary corrosion is also restricted (i.e. grain boundaries become more cathodic). As observed in Fig. 1.2(a), the as-received micrograph exhibits considerable pitting identified by the corroded patches appearing dark due to the roughness rendered by corrosion. However, the micrograph of LSM treated sample shows marked difference in the corrosion behavior, as observed in Fig. 1.2 (b), the micrograph of the LSM sample. The Figure shows preferred corrosion in the bulk grains while the grain boundary remains shiny and un-reacted as it is more electropositive than the grains.

Thus, the shift from pitting corrosion (for as-received samples) to uniform corrosion (for LSM treated samples) as inferred from the SEM microstructures is highly effective in improving the surface quality. Therefore mechanical properties can be significantly improved by LSM treatment, especially fatigue endurance and wear resistance properties as these properties are extremely sensitive to surface irregularities.

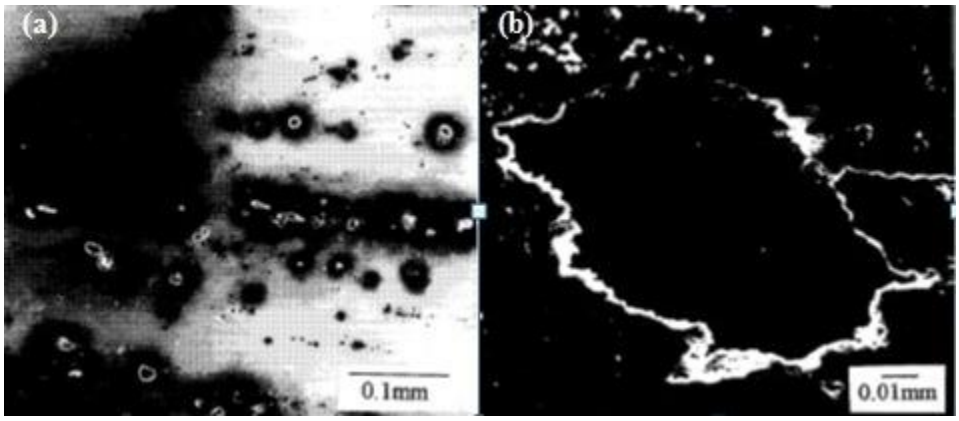

Fig. 1.2 (a) SEM micrograph of as received alloy, and (b) SEM of LSM treated alloy (printed with permission) [47]

This also marks a very uncommon and beneficial feature that the grain boundary is cathodic or more corrosion resistant than the matrix, minimizing the chances of intergranular corrosion. The Al-Cu system is often reported to show aggravated grain boundary corrosion and embrittlement, LSM offers an absolute reversal of the situation, further improving their applicability.

The studies also revealed that due to the relatively lower boiling temperature of Mg, LSM causes selective vaporization of Mg from the melt pool. Mg was undetected from the XRD tests of LSM treated samples, indicating reduction in volume of Mg-rich Al_2CuMg intermetallic phase. The selective vaporization improves the corrosion resistance by reducing the surface area of electropositive precipitates due to lower solute (Mg) concentration in the melt. The influence of the precipitates on the corrosion behavior of the alloy was studied using free corrosion experiment which records the variation of open circuit corrosion potential with time. It was observed from the studies that in an acidic or saline environment, the corrosion resistant oxide undergoes dissolution after a period of time due to enhanced pitting. This results in significant reduction of corrosion potential, rendering the surface more anodic. However, the modified microstructure achieved by LSM process causes a shift in the corrosion mechanism from pitting towards uniform corrosion. The investigation again confirmed that the stability of the LSM treated samples is very high since LSM samples, unlike the as-received samples, do not experience any breakdown of the oxide film. The variation of corrosion potential of the laser treated and base sample can be observed in Fig. 1.3.

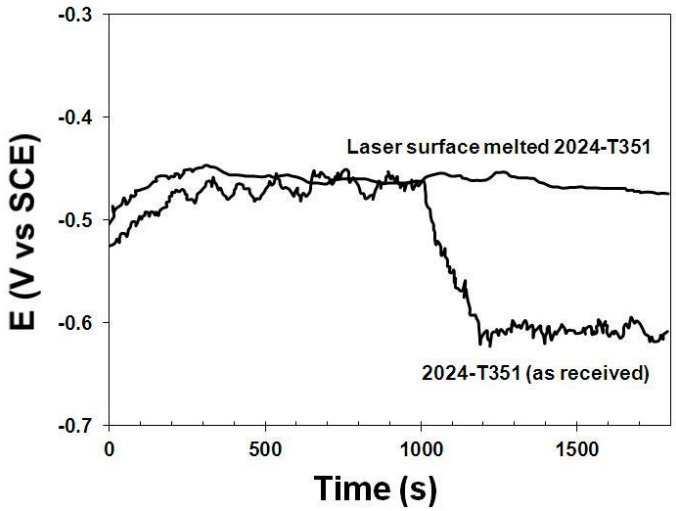

Fig. 1.3 Potential versus time curve for as-received and LSM treated samples (Adapted from [47]) (printed with permission)

This can be attributed to the variation of corrosion current density with the mechanism of corrosion in the materials. In the as-received samples, the local corrosion current density around the precipitate interfaces is higher than the bulk material. However, as the interfaces are the actual anodic sites, the entire anodic area is just a minor fraction of the bulk area. This creates rapid dissolution around the pits, initiating the breakdown of the film in as-received samples. This phenomenon also supports the observations of Liao [44], which indicated the onset of severe pitting after breakdown of the film due to initial pitting and activation of the less electronegative solute clusters. The LSM samples, however, show no breakdown due to the comparatively low corrosion current density and uniform corrosion of the bulk grains. The dissolution of oxide film is delayed as the microstructure is stabilized by the lack of precipitates, resulting in a much higher corrosion resistant surface.

The 2024 Al alloys are noted for their complex alloy composition with more than three alloying elements, and hence various precipitate composition and morphology can be achieved by altering heat treatment procedure. The effect of Mg in the microstructural evolution during LSM and its effect in pitting corrosion of 2014 and 2024 alloys was investigated by Liu *et al* [48, 49]. The 2014 alloy has chemical composition very similar to the 2024 alloy, except for much lower Mg content (2014 has 0.2% to 0.8% Mg while 2024 has 1.2% to 1.8% Mg). Hence, these alloys proved to be very effective in identifying the effect of Mg on corrosion behavior. A CO_2 laser with 1.6 kW power, 1 mm spot diameter, 15 to 180 mm/s scanning velocities, and 50% track overlap was used for the LSM treatment of the 2024 alloys. The Mg content in the precipitates was observed to decrease with decrease in laser scanning velocity.

The decrease in Mg content was because decrease in scanning velocity increased interaction time, and thereby, increasing Mg vaporization due to higher temperature in the melt. Increased vaporization of Mg lowers the concentration of Mg in the melt pool, and hence the precipitate composition was affected

(the Mg-rich Al_2CuMg phase was replaced by Al_2Cu). The pitting potential studies in 3.5% deaerated NaCl solution revealed that the Al_2CuMg phase (E_{corr} = 680 mV) is more electropositive than the Al_2Cu phase (E_{corr} = 560 mV) at identical conditions. Hence, replacement of Al_2CuMg phase with Al_2Cu phase is beneficial for corrosion resistance due to reduction in potential of internal corrosion cells. The preferential migration of Cu as compared to Mg and Si was also observed in EPMA mapping. Evidently, the higher atomic volume of Cu is more effective in reducing free volume of the grain boundaries and hence the driving force for Cu migration is considerably higher than Mg and Si, as observed in Fig. 1.4. Thus, reducing scanning velocity and thereby enabling selective Mg vaporization can effectively be used to further improve the corrosion resistance of the alloys.

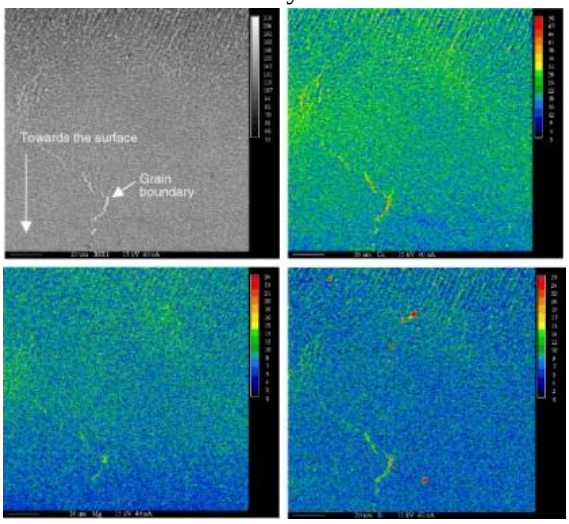

Fig. 1.4 EPMA mapping of 2014 alloys treated with LSM with a Nd-YAG laser (printed with permission) [49]

1.2.3.1.2 Precipitate Morphology

The use of LSM in binary eutectic Al-Cu system (reported to exhibit similar Al_xCu_y intermetallic precipitates observed in 2024 alloys) was investigated by Zimmerman *et al* [50]. The investigation was performed using a CO_2 laser with irradiation powers of 1 to 1.5 kW. Transmission electron microscopy was used to investigate the microstructural evolution at various laser scanning velocities. The TEM analysis revealed that the eutectic microstructure morphology varied significantly with solidification

velocity (correlated with laser beam scanning velocities) of LSM treatments. Below a solidification velocity of 20 cm/s, the Al_2Cu precipitates were largely lamellar as observed in Fig. 1.5(a). The precipitate morphology of laser treated samples above the threshold solidification velocity of 20 cm/s tended to become wavy, with the amplitudes increasing with increasing solidification velocity, as observed in Fig. 1.5(b). Above a solidification velocity of 50 cm/s, the cooling rate seemed to be too fast to allow precipitate growth, and a highly banded structure as observed in Fig. 1.5(c), parallel to the solid-liquid interface was observed. The influence of banded microstructure (developed by friction-stir welding) on the crack propagation of 2024 alloys was investigated by Sutton *et al* [51, 52].

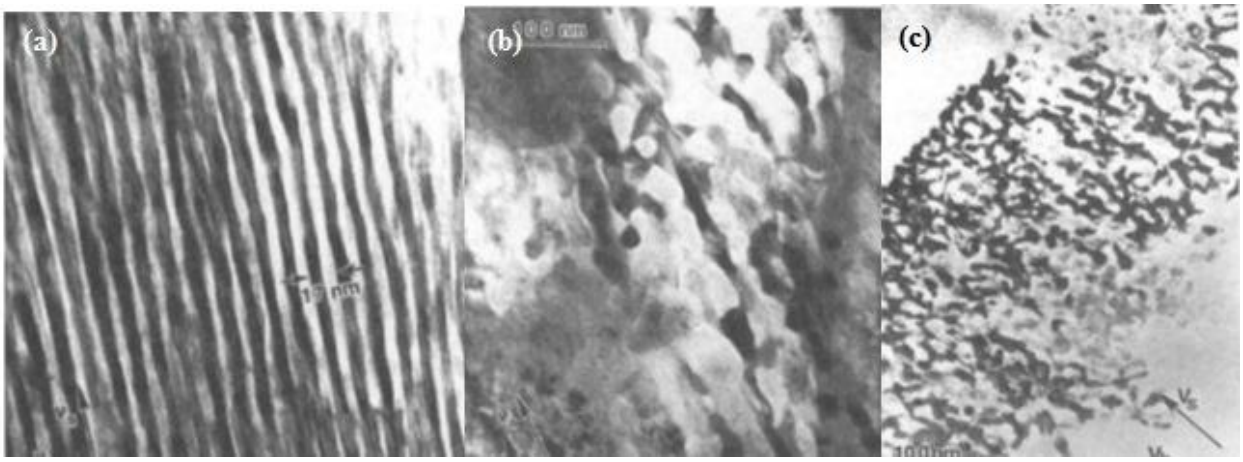

Fig. 1.5 TEM microstructures of laser surface melted Al-Cu alloys at solidification rates of: (a) 20 cm/s, (b) 20-50 cm/s, and (c) 50 cm/s (printed with permission) [50]

The investigation revealed that the increased particle density in the precipitate-rich bands strongly influence the crack-tip field during the early stages of crack growth. The increase in particle density increases the statistical probability of an advancing crack to encounter a particle, and thereby triggering crack branching. Hence this feature can be used as an effective toughening mechanism, especially in improving fatigue endurance. Thus, laser surface melting not only offers the scope to develop finer and more refined microstructures, but also control the morphology of the precipitates by optimization of the laser scanning velocity. Hence, superior control of the mechanical and surface properties can be achieved

as optimization of LSM input parameters is highly effective in developing desired properties required for specific applications.

1.2.3.2 Laser Composite Surfacing (LCS) of AA 2024 Al alloy:

The 2024 Al alloys are extremely sensitive to heat treatments, and very high ratios of peak strength to solutionized strength can be achieved in these alloys. Hence, although LSM of these alloys improve corrosion resistance, it also decreases precipitate density due remelting of laser-irradiated regions and restricted ageing time for precipitation. The reduced precipitate density often results in drastic reduction of the strength and wear resistance in the laser modified surface. Ceramic particles such as TiC, SiC, and Si_3N_4 are noted for their very high hardness and abrasion resistance. LCS of 2024 Al alloys using these hard particles is gaining significant importance to improve the surface hardness. LCS of Al alloys with these hard ceramic particles have reported to exhibit notably higher hardness and wear resistance by various research groups [53, 54]. Also, apart from using ceramic particles exclusively, hybrid composite surfacing with mixtures of metal and ceramic particles has been attempted. The improvement in wear resistance has been reported to depend on factors such as surface hardness, size and dispersion of particles, and particle-matrix bonding strength. Hence, research endeavors have not only targeted different hard particles for reinforcement but also identified additives to improve wettability of the particles, thereby, improving bonding strength.

1.2.3.2.1 LCS with TiC particles

LCS of the 2024 Al alloys using TiC powders was investigated by Kadolkar and Dahotre [53]. Their studies revealed that except for very high laser scanning speeds beyond 200 cm/min when diffusion is severely constrained, the particle-matrix bonding is generally very good in 2024 alloys composite surfaced with TiC. This good particle-matrix bonding can be attributed to the comparatively high Cu concentration (4 wt.%) in the 2024 alloys, as Cu significantly improves the wettability of TiC [55]. The

authors reported injecting a mixture of ceramic particles and silicon powder with a weight ratio of 9:1 in the melt pool. The addition of silicon was to enhance the wettability of the particles in the melt zones. The microstructural characterization showed the existence of three distinct zones: the coating zone, the heat affected zone, and the base alloy zone, as observed in Fig. 1.6(a). A marked increase in Knoop hardness from about 100 kg/mm^2 for the substrate to 350-400 kg/mm^2 at the surface was observed due to the ceramic reinforcement (Fig.1. 6(b)).

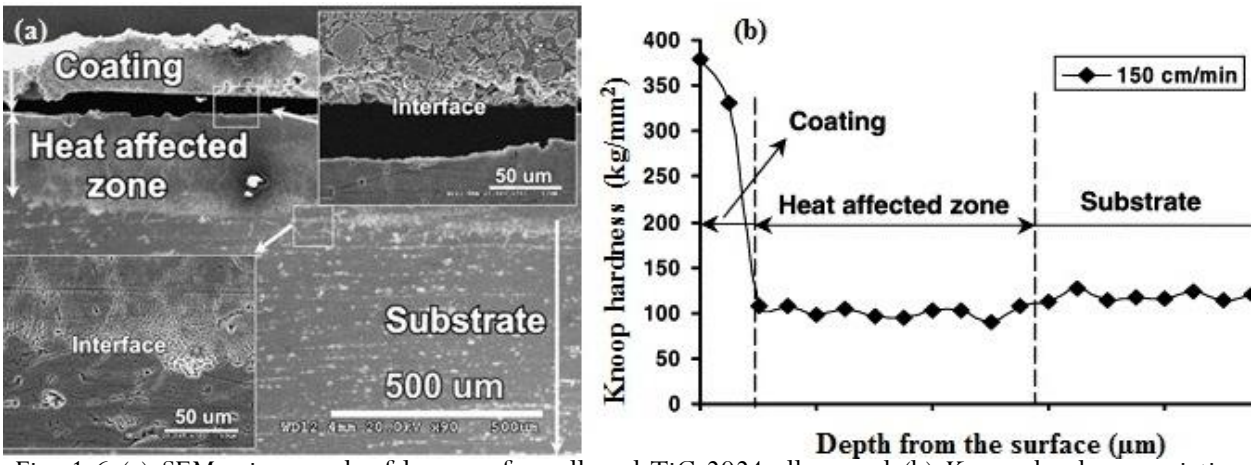

Fig. 1.6 (a) SEM micrograph of laser-surface alloyed TiC-2024 alloy, and (b) Knoop hardness variation with depth (printed with permission) [53]

1.2.3.2.2 In-situ LCS

The traditional LCS, as discussed, involves injecting hard particles in laser melt pool. Other novel approaches have also been attempted to develop *in-situ* composites at the surface using laser irradiation, as *in-situ* composites often exhibit superior bonding strength between matrix and particles. The approach for developing *in-situ* metal matrix composite coating on 2024 alloys was reported by Xu *et al* [56]. The reinforcement particles were formed *in-situ* due to intermetallic reactions triggered by the injection of Fe-coated B, pure Ti, and pure Al powders in the laser melt pool. The input parameters in the investigation were CO_2 laser power of 1.7 kW and scanning velocity of 3 mm/s. The surface oxidation was prevented

using a coaxial jet and side jet of Ar. A distinct relationship of the wear resistance with the applied load was observed by the authors. When the applied load was low (8.9 N), the wear resistance and hardness of the composite surfaces of the alloys increased with increasing volume percentage of TiB_2, Al_3Fe, and Al_3Ti dispersions. This can be explained from the fact that the dispersed particles acted as higher load-bearing phases, preventing the base Al-matrix from getting loaded by the wear balls. However, as the loads were increased (17.8, 26.7, and 36.9 N), the wear behavior changed and aggravated wear was observed with higher volume fraction of dispersion phases. It was concluded that increasing loads increased particle-matrix strain thereby causing pulling out of reinforced particles. The wear debris of pulled out hard particles initiates third-body abrasive wear on the material surface, significantly deteriorating the wear resistance of the material. Hence, careful material selection and processing techniques should be used, as the wear resistance not only depends on the particle distribution and volume percentage, but also the applied load.

1.2.4 AA6061 Alloys

The 6061 Al alloys are one of the most popular commercial alloys of the 6xxx series Al alloys. The typical chemical composition of 6061 alloys has been reported in Table 1.2 [31]. The 6061 alloys are reported to be the preferred materials for applications in general purpose structural, passenger railroad cars, movable radio telescopes [57]. The distinguishable properties of these alloys are its superior corrosion resistance, stress corrosion cracking resistance, weldability, and formability compared to other PHA alloys. The cost of production for 6061 alloy is relatively lower than that for 2024 alloys due to the greater availability of Si compared to Cu. Hence, the popularity of 6061 alloy often supersedes the 2024 alloy although the maximum peak aged strength achievable is only about two-thirds of the strength of 2024 systems, as observed from Table 1.3 [58].

The 6xxx series alloys are unique because this is the only Al alloy system that consists of two principle alloying elements: Mg and Si. Interestingly, although Mg and Si are also the principle alloying elements of the 4xxx and 5xxx alloy system, respectively, the 4xxx and 5xxx series are non-heat treatable. The lack of heat treatability is primarily due to the sharper slope of the solvus lines of Al-Si [59] and Al-Mg [60] which renders their corresponding alloys unsuitable for heat treatment. However, the unique interaction of Mg and Si in Al matrix produces Mg_2Si precipitates and enables the 6xxx alloy systems heat treatable [61]. As these 6061 alloys have relatively lower strength in the PHA alloy group, most of the LSE efforts are focused on improving surface mechanical properties.

1.2.4.1 Laser Surface Melting (LSM) of AA 6061 alloys

LSM of 6061 alloys is a rather unexplored unlike LSA and LCS of these alloys. This lack of interest in LSM appears to be due to the inherent high corrosion resistance of 6061 alloys, making further LSM operations to improve corrosion resistance redundant. However, the results reported in the limited attempts on LSM of 6061 alloys are rather promising, and quite a few breakthroughs in this field can be predicted in future.

The effect of LSM using a high power Nd-YAG laser on the electrochemical properties of 6061 alloys was investigated by Weinman *et al* [61]. The laser with pulse energy of 111 J, pulse time of 1.2 ms, and defocused spot diameter of 4 mm diameter was used in an air or helium environment. The surface microstructure after LSM showed existence of three zones reminiscent of weld microstructures: the melt zone, the heat affected zone, and the base material. The SEM characterization showed cracking at the interfaces of inclusions and matrix in the melt zones. Porosity in the melt structure was also observed. In the fracture studies of the LSM samples, surface cracks appeared to grow preferentially along the pores. The reason for the cracking and porosity in the melt matrix was deduced to be governed by the extremely high cooling rates generated during laser processing and the limited time for the dissolved hydrogen in the

melt to escape. The extraordinary cooling rates generate intense thermal stress during the processing, and the hydrogen is generated due to reduction of water vapor by the Al in the melt. The investigations of Delogu *et al.* on the melt zone of 6061 alloys created during laser welding operations also confirmed the presence of hydrogen [62]. The solubility of hydrogen in Al was reported to be influenced by the alloying elements present in the melt. For example, while Cu decreases hydrogen solubility in Al, Mg increases it. Therefore, the presence of Mg as a premier alloying element in 6061 also enhances porosity formation as Mg increases hydrogen content in the melt.

The influence of LSM on corrosion resistance of 6061 alloys was investigated by Man *et al* [54]. The corrosion resistance experiments were performed in a de-aerated solution of 3.5% NaCl solution, and temperature was maintained at 23°C. The SEM microstructural investigation revealed intense pitting in the base materials, especially at the electropositive Mg_2Si precipitate and matrix interfaces. The corrosion potential showed mild improvement of 32 mV in LSM treated samples due to the highly uniform surface of the laser treated samples. But, no notable improvement in pitting potential was observed.

1.2.4.2 Laser Surface Alloying (LSA) of 6061 Al Alloys

The 6061 Al alloys, as mentioned earlier, have superior corrosion resistance, weldability and formability than 2xxx and 7xxx alloys. But the alloy's popularity is affected by its comparatively lower strength and wear resistance. Hence, LSA of this alloy has gained immense interest in recent research to address the comparatively lower hardness and wear resistance.

1.2.4.2.1 Alloying with Ni and Ti

Alloying of 6061 alloys with metals using LSA and their effect in wear and corrosion behavior has been successfully demonstrated by several research groups. Wear response of 6061 alloys surface alloyed with Ni and Ti powders was investigated by H.C. Man *et al.* using a Nd:YAG laser with a laser power of 1.5 kW [63]. The microstructural investigations revealed formation of very hard intermetallic

aluminides and titanides such as Ni_3Al, Al_3Ti, NiTi, and TiAl. The alloy surfaces after LSA showed marked improvement in wear resistance compared to the original base alloy, with the mean wear rates of $3.75 \times 10^{-5}\,cm^3\,h^{-1}$ and $21.25 \times 10^{-5}\,cm^3\,h^{-1}$ for the LSA samples and base alloys, respectively. The more than five-fold improvement in wear resistance for the LSA surfaces was inferred due to a transition in the wear mechanisms. The base alloy being soft and ductile, undergoes extensive plastic deformation and initiates adhesive wear, and thereby, accelerates the wear process. However, the formation of very hard intermetallic particles in the ductile matrix during the LSA operation generates an almost-perfect condition for wear resistance. The wear mechanism is primarily abrasive wear as inferred from the remarkably smoother wear tracks. The hardness also showed considerable improvement from 100 HV to 350 HV. The surface modification was achieved for an appreciable thickness of 1.5 mm. It has been reported that efficiency of power absorption increases with decreasing wavelength resulting in higher depths of alloying [64]. Therefore, the comparatively higher laser melt thickness is most likely due to the shorter wavelength of Nd:YAG lasers (of 1.06 μm) as compared to CO_2 lasers (10.64 μm). Also, studies of aluminide formation have reported these reactions to be intensely exothermic and can contribute in increasing the laser melt zone size [65, 66].

1.2.4.2.2 Alloying with Ni and Cr

Ni is reported to form tough and very hard aluminides. Thus, surface alloying of Al alloys with Ni can potentially produce excellent surface hardness and wear resistance. However, LSA has been reported to induce surface porosity due to H_2 evolution associated with reduction of water during laser surface treatment [61, 62]. Hence, the influence of input parameters during LSA of 6061 alloys with Ni and Cr as alloying elements on cracking and porosity of resolidified region was investigated by Fu *et al* [67, 68]. The studies involved understanding the influence of laser power on the cracking of the laser treated zone during the processing, and thereby optimizing the laser input parameters such as incident power, scanning velocity and overlapping ratio. The studies were performed using a Nd:YAG laser, and a

mixture of commercially available Ni and Cr powders in a ratio of 7:3. The powder mixture was sprayed on the substrate using plasma spraying technique before laser alloying. The cracking and porosity were then analyzed using image processing software. The investigation concluded that each parameter has a very critical influence in the cracking and porosity of the laser treated zone. Low incident power generates a very thin and inconsistent surface layer, while very high power showed extensive porosity and microcracking due to the huge thermal distortion generated by high input thermal energy. Similarly, very low scanning velocity enhanced surface roughness making the materials highly unsuitable for high fatigue endurance applications or applications that require very high surface finish such as automobile bodies. The surface roughness is generated due to the increased time for power absorption, creating depressions on the surface. Again, very high scanning velocities reduced the overall interaction time of the laser on the substrate, therefore restricting time to allow the entrapped gases to escape, creating defects such as pinholes. The laser track overlapping also influences the cracking of the material because greater overlapping generates greater distortion and hence material becomes more susceptible to cracking. Lower track overlapping essentially renders the surface with highly heterogeneous properties, as laser surface treatment generates a semicircular melt region which narrows at the edges. The analysis of these three parameters and cracking concluded the existence of an optimized regime of input parameters where the most favorable results were observed, as depicted in Fig. 1.7 (a).

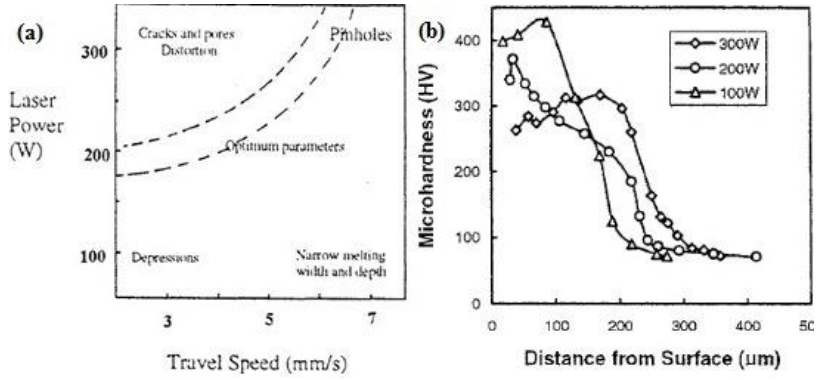

Fig. 1.7(a) Influence of laser parameters on processing defects during laser surface alloying of 6061 alloy, and (b) variation of hardness with input laser power (printed with permission) [67]

The surface hardness was reported to increase from 50-60 HV in base alloy to about 400 HV in the alloyed surfaces at a laser power of 100 W. As Fig. 7 (b) shows, laser power had an inverse relationship with surface hardness as increasing incident power triggered increased the dissolution of alloying metals (Ni and Cr). Increasing dissolution decreases the volume fraction of the hard intermetallic phases, detected to be primarily Ni_3Al by the XRD techniques, formed due to the surface alloying. Interestingly, although Al has very low solubility of Cr [69], the presence of Cr in the intermetallic phases was undetected. Probably the precipitation kinetics of Cr-based intermetallic compounds of Al was highly constrained and the presence of Ni may act as a stabilizer, enhancing the solubility of Cr in Al.

The studies also involved understanding the influence of LSA in the fretting wear behavior of the 6061 Al alloy [69]. The variations in coefficient of friction, maximum wear depth, and fretting wear volume were studied to characterize fretting wear loss. The experiments showed a distinct drop in the coefficient of friction, due to the presence of harder Ni_3Al intermetallic phases. These hard improve surface smoothness during wear, and thus minimize adhesion of substrate with the wear balls. The wear resistance showed appreciable improvement in the LSA samples. The wear tracks were studied using microscopy techniques, which revealed extensive plastic deformation in base material. Oxidative wear was also observed as the wear debris eventually oxidizes to hard Al_2O_3 particles, as detected in the wear scars, and further deteriorating the wear phenomenon. Hence, the wear mechanism undergoes a transition with time, initially being adhesive and abrasive wear due to high amount of plastic deformation on the surface. But, with time, the wear phenomenon shifts to oxidative wear, and the rate of oxidation determines the wear rate. In either case, the hard intermetallic phases are extremely effective in slowing wear rate as the appreciable hardness and surface smoothness reduces the coefficient of friction and subsequently adhesive wear of the material. Also, the high electropositivity of the Ni_3Al makes them less susceptible to oxidation, and hence, the oxidative wear is restricted due to lower oxide formation [70].

1.2.4.2.3 Alloying with Co and Cr

In the investigations of the phases formed during LSA of 6061 alloys with Ni and Cr, no intermetallic Cr-based phases were reported. However, Cr-based intermetallic phases were observed after LSA of 6061 alloys with Co and Cr by Chuang *et al* [71]. The LSA was performed using a 5 kW CO_2 laser with a Co-Cr alloy of weight ratio maintained at approximately 7:3 and fed with a rate of 2 g/min. The beam was defocused to a diameter of 2.5 mm, and the laser scanning velocity was maintained at 10 mm/s. It was noted in this investigation that porosity could be avoided during this laser treatment process. But, the higher density and melting point of the alloying elements (Co and Cr) caused non-uniform elemental distribution in the resolidified zone; the concentration of alloying elements was observed to increase with depth, as shown in Fig. 1.8(a). Internal stress was also observed due to the relatively slower solidification rates of at the core of the melt pool, triggering cracking as observed from the microstructural studies. The lack of driving force for precipitation of Cr in the base metal in spite of its low solubility, similar to the observations of Fu *et al.* [67, 68], was again reported in this study. Also, a transition in the chemical composition of the Al-Co precipitates with depth was detected. In the microstructural investigation, due to the lower availability of Co in the shallow regions of the melt pool, significant presence of the smaller and lower Co content Al_9Co_2 phases was detected. However, the deeper and more concentrated regions primarily yielded the richer and considerably larger phases, notably $Al_{13}Co_4$ and Al_7Cr.

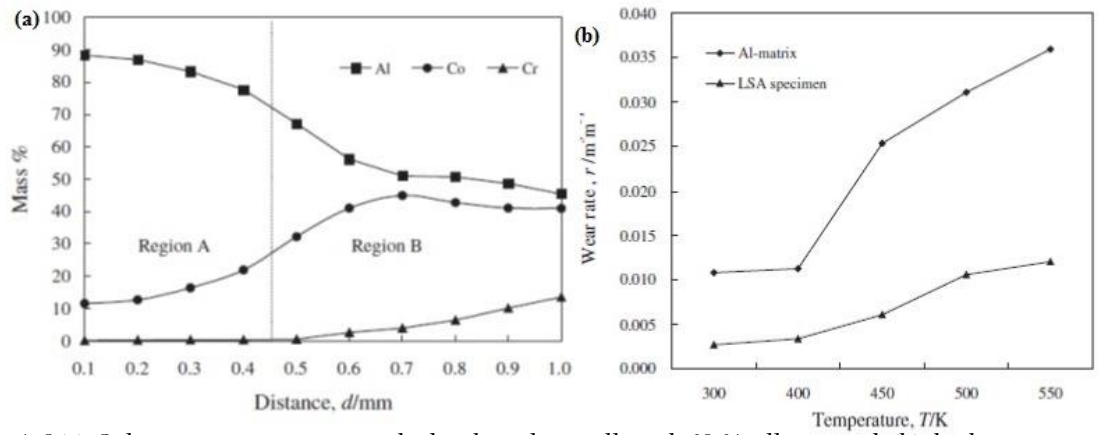

Fig. 1.8(a) Solute concentrations with depth in laser alloyed 6061 alloys, and (b) high temperature wear response of base and laser alloyed samples [71]

The influence of the unique variation in hardness on the surface properties was established with in the high temperature fretting wear studies (Fig. 1.8(b)). The wear behavior was reported to be primarily adhesive wear with extensive plastic deformation of the base material in the wear scars. The increase in coefficient of friction due to greater plasticity and adhesion at higher temperature exacerbated this wear phenomenon; significantly increasing wear rate at higher temperatures for the base material. However, the laser alloyed samples exhibited much higher wear resistance at elevated temperatures due to presence of the extremely hard subsurface layer. With increase in temperature, the comparatively softer surface (with Al_9Co_2-rich phases) is worn off. But, eventually the fretting wear rate decreased as the denser and harder $Al_{13}Co_4$ and Al_7Cr phases, which were subsequently exposed after removal of Al_9Co_2 rich layer, could withstand the aggressive high temperature fretting conditions. Hence, although the wear resistance aggravates considerably with temperature in base alloy, it was observed to be largely unaffected in the laser modified samples.

1.2.4.3 Laser Composite Surfacing (LCS) of 6061 alloys

1.2.4.3.1 Composite Surfacing with SiC and Si_3N_4

The use of hard ceramic particles as reinforcements in metals has been of considerable interest, and therefore, forming metal matrix composites is often cited as one of most promising design approaches to attain superior mechanical properties in conventional materials. The 6061 alloys having relatively lower strength when compared to other PHA alloys are well suited for LCS studies. H.C. Man *et al.* investigated the effects of additions of SiC and Si_3N_4 as reinforcement particles in 6061 alloy [54]. The LCS was performed using a Nd:YAG laser with a power of 1200 W and defocused beam spot diameter of 3 mm. The ratio of SiC:Si_3N_4 was varied to conduct a comparative study, and thereby, quantify the effect of reinforcement particles. The cavitation erosion was studied by determining material loss in a saline environment of 3.5% NaCl at a temperature of 23°C. The results revealed that while Si_3N_4-reinforced samples had a profound effect in improvement of cavitation erosion of these materials, the effect due to composite surfacing with SiC-reinforced samples was only slightly better than the base alloy (the erosion resistance for Si_3N_4-reinforced samples increased by three times compared to base Al alloy). Also, the alloys prepared using both SiC+Si_3N_4 yielded intermediate properties, better than pure SiC-reinforced samples but inferior to pure Si_3N_4-reinforced samples, which again underlined the efficiency of Si_3N_4-reinforced samples against SiC-reinforced samples. It should be noted that cavitation is the combined effect of both erosion as well as corrosion. Hence, although the creation of additional particle-matrix interface lowers the corrosion resistance of the materials, the cavitation resistance circumvents this issue owing to much increased surface hardness. In the microstructural examination, it was observed that the samples after LCS had good metallurgical quality and the modified surfaces were free from defects such cracks and porosity. The remarkable improvement in Si_3N_4-reinforced samples was determined in the microstructural studies and erosion mechanism. The relatively lower volume fraction of reinforcement particles in wear debris was deduced due to extensive plastic deformation and subsequent plastic rupture

of the soft and ductile matrix, while the unusually harder reinforcements were not deformed. The nucleation and growth of the voids were observed to have initiated from the particle-matrix interfaces. Hence a stronger interface was the key to superior cavitation resistance. The microstructures revealed that while SiC had a largely simple polygonal shape, the Si_3N_4 particles had a highly irregular clustered shape. The larger particle-matrix interfacial area for Si_3N_4 particles significantly increases the interfacial bonding, resulting in much higher erosion resistance.

1.2.4.3.2 Composite Surfacing with TiC

The effect of LCS of 6061 alloys with TiC was studied by Katipelli *et al* [72]. The LCS was performed using a Nd:YAG laser with a laser power of 1800 W, laser scanning velocity of 2 mm/s speed, and defocused beam diameter of 0.5 mm. The laser parameters were adjusted to considerably high power regimes to involve surface melting on the laser irradiated region. The laser irradiations also caused partial melting of the ceramic powders, enhancing wetting at the particle-matrix interface. The wetting was further improved by using a mixture of TiC particles and Si powder in a ratio of 9:1 by weight. Si is known to reduce the viscosity of molten Al and thus improves wettability [73]. The intermetallic phase formation after LCS was subsequently characterized using XRD techniques and was also analyzed using theoretical thermodynamic calculations. Each of the phases detected (TiC, SiC, $TiAl_2$, and $TiAl_3$) was predicted from its thermodynamic driving force by free energy calculations. However, Al_4C_3 phase was not detected in the characterization studies even though it was predicted among the possible phases in the thermodynamic study. The absence of this phase was hypothesized because of the scarcity of adequate free Si in the melt pool. Although only 8% Si is required for a stable carbothermic reduction of SiC and the amount of silicon added was 10%, the reaction appeared to be unstable since entire Si was not active for reactions. Similarly, only traces of $TiAl_3$ form only at very low concentration of carbon or very high concentration of titanium. The samples after LCS exhibited higher roughness than the base materials. The

wear resistance of the laser treated materials showed appreciable improvement, underlining the efficiency of the LCS treatment in wear-intensive applications.

1.2.4.3.3 Composite Surfacing with Ceramic and Metal Mixtures

One recurring feature about composite surfacing of Al alloys, as discussed from the works of Man [54] and Katipelli [72], is the low particle-matrix bonding strength. The weak particle-matrix interfaces act as nucleation sites for voids, and therefore, Si addition for superior wettability was required to achieve superior interfacial bonding during LCS. Hence, various combinations of ceramic particles and metallic additions have been attempted to achieve superior interfacial bonding, which presumably is the most critical factor to improve surface properties.

The investigations on hybrid particle-metal addition during LCS were reported by Man *et al* [74]. LCS of 6061 alloys was conducted using Ni+Al and Ni+Al_2O_3 feed powders. Also, a 0.3 mm layer of varying compositions of Ti, C, W, and WC was pasted on the substrate prior to LCS. A Nd:YAG laser with incident beam power of 1.6 kW, spot size of 1.6 mm, powder feed rate of 24 g/min, scanning velocity of 20 mm/s, and 50% track overlap was used for LCS. The motivation for the addition of pure elements like Ti, C, and W was to facilitate in-situ reactions in the melt pool. The samples prepared with Ni+Al_2O_3 feed powder and pre-pasted layer of Ti, C, and WC generated phases such as Al_2O_3, TiC, WC and Al_3Ni_2 after LCS. In samples with identical feed powder composition (Ni-Al_2O_3) and pre-pasted layer of W and C, presence of Al_2O_3, TiC, WC, Al_3Ni_2, Al_3Ni, and Ni phases was detected. The other set of experiments, where Ni+Al was used as a feed powder and samples pre-pasted with WC or W+C, showed presence of TiC, WC, Al_3Ni_2, and Al_3Ni. Mild porosity was also observed in the samples, most likely due to the oxidation of C to CO_2. An exceptional improvement in hardness was observed in samples after LCS treatment, with hardness of base material increasing from 80 HV to 800 HV (for Ni+Al feed powder, and Ti, C, and W pasted layer) and to 1100 HV (for Ni+Al_2O_3 feed powder, and Ti, C, and WC pasted layer).

The wear response also followed similar trend, with Al_2O_3 injected powders showing improved wear resistance than Al-added samples due to inherent high hardness of Al_2O_3. Also, in-situ particle formation was explained as a consequence of the high temperatures (about 2350°C) reached due to the laser surface irradiation. The high temperature results in the dissolution of C in Ti, and thereby, triggering highly exothermic TiC formation reaction. It was also observed that LCS using Ti, C and WC (instead of uncombined Ti, C, and W) resulted in better properties. This seemed to be due to mildly exothermic nature of WC formation reaction compared to TiC reaction. Hence, WC formation is triggered only after very high temperature is reached for TiC reaction, thus restricting *in-situ* WC formation.

The applicability of LCS using Mo powder and WC as reinforcement particles on 6061 alloy was studied by Chong *et al* [75]. Metals such as Ni and Mo are noted for their ease of formation of corresponding high melting metal aluminides. Also, interfacial bonding of particle and matrix is particularly favored when the particle-matrix interface is diffused. Due to the considerably higher melting point of the metal aluminides, the difference in melting point of WC particles and aluminides of Mo is significantly smaller than the difference in melting point of Al and WC particles. Therefore, it was predicted that the similar melting points will improve simultaneous melting of the phases to yield continuous and stronger metallurgical bonding among the microstructural phases.

The study was performed using a Nd-YAG laser with an incident power of 1.4 kW, scanning velocity of 17 mm/s, and defocused beam diameter of 1 mm. The overlapping on a laser track was maintained at 50%, and surface oxidation was avoided by use of co-axial and side jet of argon gas. The mixture of Mo and/or WC powders was pre-placed using 4% poly-vinyl alcohol to a thickness of 1 mm on the substrate. The phases characterized in the melt zones after LCS were Al_5Mo, $Al_{22}Mo_5$ and $Al_{17}Mo_4$ in pure Mo-alloyed samples. For the samples alloyed with both Mo and WC, additional phases such as Mo_2C, Al_4C_3, WAl_{12} and WC were identified. A considerably diffused interface, inferring the interface to

have extensive interfacial bonding, was observed, as reported in Fig. 1.9(a). Excellent metallurgical soundness without any cracking and porosity was observed from the microstructural investigation. Also, a drastic reduction in the melt zone thickness was noted in WC and Mo alloyed samples. While the WC and Mo alloyed samples showed a melt zone thickness of 150-250 µm, a melt zone thickness as high as 430 µm was observed in the pure Mo-alloyed samples. The analysis of such substantial influence in melt zone thickness was conjectured due to the result of the significant reduction in thermal conductivity of the 6061 substrate on addition of WC powders. The characterization also revealed that the matrix was primarily Al-Si alloy system; a plausible explanation might be due to the selective vaporization of low boiling point Mg similar to the results of Li *et al.* [47] in 2024 alloys. Also, similar to the results reported by Chuang *et al.* [71] with LSA of 6061 alloys with Cr and Co, inhomogeneous distribution of reinforcement phases due to disparity in density was observed. The lower region of the melt zone was observed to have a higher concentration of heavier WC particles than the upper region. A relation of the weight ratio of Mo/WC added to the melt pool and the particle distribution was noted. The homogeneity of particle distribution was observed to increase with increase in WC volume fraction. Hence apparently the melt zone depth decreases with increasing WC particles in the melt, increasing the cooling rate. The higher cooling rate renders lower settling time to the particles and thus, particle homogeneity increases with increasing WC volume. The wear tests of the samples were performed using a pin-on disc abrasive wear apparatus. It was observed that the wear resistance improved with WC ratio in the melt. The cause for this improvement in the wear was reasoned due to the superior load bearing capability of the hard WC and intermetallic phases. However, intense plastic deformation in the matrix was observed in the WC-rich samples which triggered microvoid nucleation at the particle-matrix interfaces. Cracking at the worn surfaces was also noted at the overlapped regions of the tracks samples, due to their lower melt zone depth resulting to lower strength, as observed in Fig. 1.9(b). Thus, using pure WC for composite surfacing is not a very recommendable practice, as their lower melt zone depth makes the modified layers more vulnerable to be

worn off owing to cracking in the overlapped regions. Summary of the phases formed during LSA and LCS of PHA alloys is presented in Table 1.4.

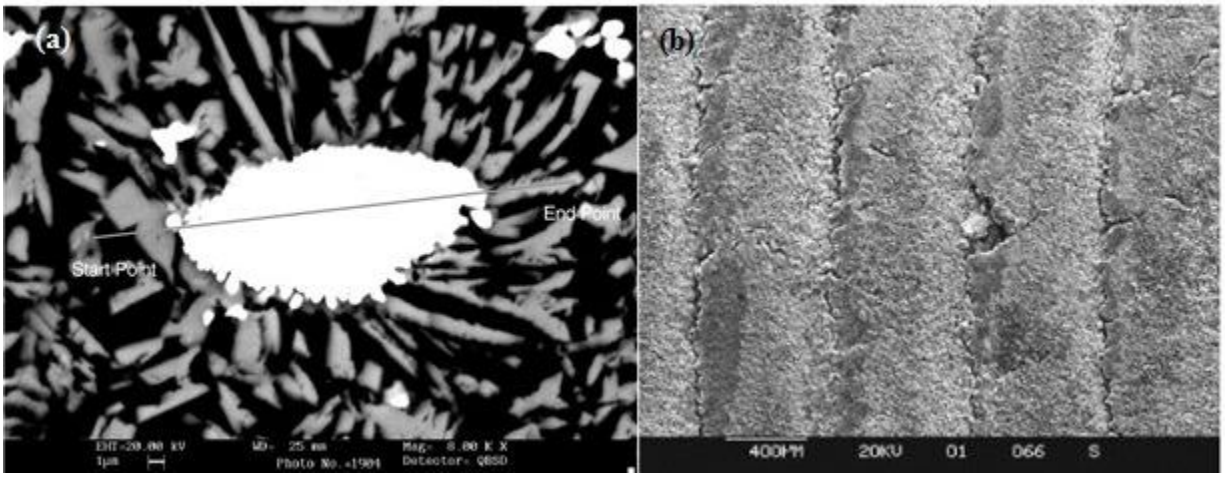

Fig. 1.9 (a) SEM micrograph of 40%WC and 60% Mo composite faced sample, and (b) Cracking at overlapped laser tracks (printed with permission) [75]

1.2.5 AA7075 Alloys

The 7075 alloy is one of the popular most materials of the 7xxx series of Al alloys. The 7075 alloys are particularly popular in aerospace industries for the past forty years [76, 77]. The typical composition of 7075 alloys is given in Table 1.2 [31]. The 7xxx alloys are reported to give the highest strength among the Al wrought alloy family [78]. This is one of the most important factors in alloy selection requiring very high strength to weight ratio. However, despite their superior strength, the 7075 are often reported with poor corrosion resistance and stress-corrosion cracking resistance [79]. Therefore, LSM can potentially be one of the most appropriate solutions to address the comparatively higher corrosion susceptibility of the 7075 alloys. Hence, several scientific investigations have been performed to establish the efficiency of LSE in these alloys.

Table 1.4 Summary of phases reported due to laser surface alloying and laser composite surfacing of PHA alloys

Alloy	Constituents added	Phases detected
2024	Fe-coated B, pure Ti, pure Al [56]	TiB_2, Al_3Fe, and Al_3Ti
	Ni and Ti [63]	Ni_3Al, Al_3Ti, NiTi, and TiAl
	Ni and Cr [67, 68]	Ni_3Al
	Co and Cr [71]	Al_9Co_2, $Al_{13}Co_4$, Al_7Co
6061	TiC and Si [72]	TiC, SiC, $TiAl_2$, $TiAl_3$
	Ti, C, TiC, W, WC, Ni, Al, Al_2O_3[74]	TiC, WC, Al_3Ni_2, Al_3Ni, Al_2O_3, Ni
	Mo and WC [75]	Al_5Mo, $Al_{22}Mo_5$, $Al_{17}Mo_4$, Mo_2C, Al_4C_3, WAl_2, WC
7075	SiO_2,Fe_2O_3, CuO, Cr_2O_3, and TiO_2[83]	α-Al_2O_3, γ-Al_2O_3, corresponding metal aluminides

1.2.5.1 Laser Surface Melting (LSM) of 7075 alloys

The effect of LSM on corrosion fatigue of AA 7075-T651 alloys was investigated by Chan *et al* [77]. The laser treatment was performed using an excimer laser with energy fluence in the range of 3.3-15.4 J/cm^2, beam spot size of 0.6 mm, and track overlapping ratio of 50%. The pulse duration of 25 ns and laser pulse frequency of 10 Hz were used for LSM. The as-received and LSM treated samples were subjected to immersion testing (immersed in a solution of 57 g NaCl and 10 ml H_2O_2 in one liter of distilled water for 48 hours) and corrosion fatigue tests in 3.5% NaCl solution. The immersion treatment was performed to aggravate pitting and thereby study the effect of corrosion pits in fatigue strength. The immersion studies revealed that while very well defined corrosion pits were observed in as-received samples, pitting was highly constrained in laser treated samples. The pitting in as-received samples was initiated along the interfaces of second phase particles (both cathodic Al-Cu-Fe-Zn and anodic Al-Mg-Zn

particles). The pitting corrosion advanced along the stringers of these particles to the depth of about 250 μm. It was observed that the elimination of second phase particles due to remelting in LSM samples resulted in formation of continuous passivation film, rendering them better pitting resistance. A very interesting and unusual observation was noted in the fatigue and corrosion fatigue tests. While the fatigue strength of the LSM samples manifested mild deterioration, the corrosion fatigue strength increased by 30%-50% for the LSM samples. This behavior was attributed to the highly rough surface associated with laser processing. Also, surface defects like porosity act as fatigue crack nucleation sites, reducing fatigue strength. However, in corrosion fatigue experiments, the sharp corrosion pits in base materials supersede the effects of surface porosity and rough surface, as the refined grain structure and highly homogeneous surface microstructure significantly improves corrosion resistance of these materials. But an extraordinary rise in corrosion fatigue strength, more than two orders of magnitude higher than base material corrosion fatigue endurance, was observed in shock-peened LSM samples as depicted in Fig. 1.10(a) and (b), respectively.

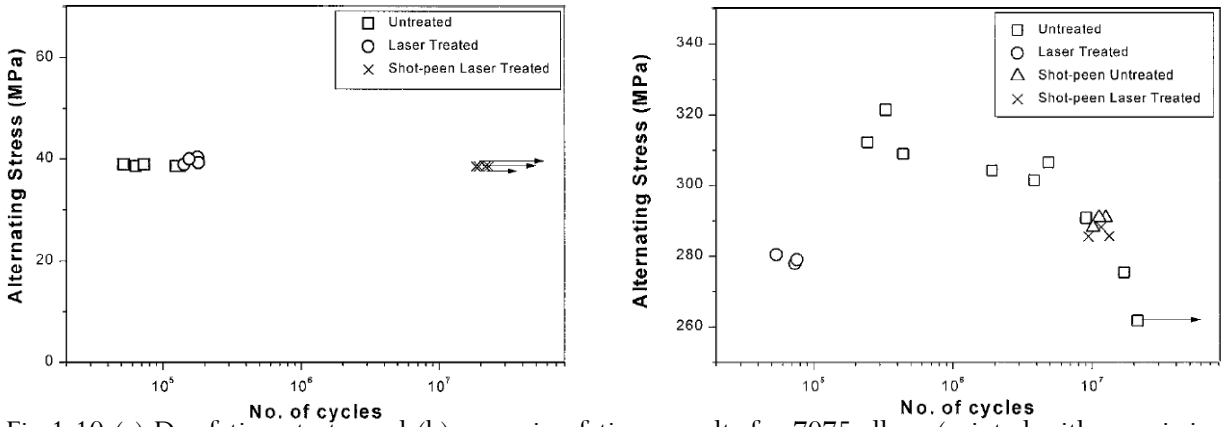

Fig.1.10 (a) Dry fatigue tests, and (b) corrosion fatigue results for 7075 alloys (printed with permission) [77]

The extraordinary improvement can be extrapolated from the fact that shock peening incorporated compressive stress on surface as well reducing surface porosity, considered as the most critical features in fatigue endurance strength. The 7075 alloys, as mentioned earlier, are frequently accompanied with poor stress-corrosion cracking (SCC) resistance. Accordingly, the immense potential of LSM in improving corrosion resistance naturally increases expectations of enhanced SCC strength from laser treated materials. The effect of LSM on SCC of 7075 alloys was reported by Yue *et al* [27]. The LSM was performed on 7075-T651 alloys using a KrF laser with the pulsed laser beam defocused to a diameter of 0.8 mm, the pulse duration of 25 ns, and frequency of 20 Hz. The SCC tests were performed by immersing the specimens in a 3.5% solution of NaCl for 20 and 30 days. The characterization of mechanical and electrochemical properties was conducted using a three point bend test and electrochemical impedance tests, respectively. The base material showed intense grain boundary corrosion, and about 1 mm crack length was observed in 30 days immersed samples. However, the laser treated materials corrosion response was highly restricted and concentrated mainly in the grain interior instead of boundaries. The considerable shift in corrosion rate was explained from Cu mapping using EBSD which showed intense precipitation of coarse precipitates at the grain boundaries in base material. Cu has been reported to improve corrosion resistance in 7xxx alloys [80]. Hence precipitation of Cu not only increases cathodic phases, but also the depletion of copper from the matrix imparts a synergistic effect to aggravate grain boundary corrosion in base material. However, the highly non-equilibrium solidification almost completely negates migration and eventual precipitation of copper at the grain boundaries in LSM treated samples. In contrast to the base material, the TEM study revealed the absence of the highly electropositive η precipitates at grain boundaries in laser treated samples, thus reducing the preferential corrosion site at the grain boundaries. The influence of the shift of mechanism from grain boundary corrosion (as-received samples) to more uniform corrosion (LSM treated samples) in passivation was demonstrated using the EIS studies. In the EIS studies, more than 5 times increase in

surface resistance was observed for the laser treated samples. This was attributed to the presence of a uniform passive layer and lack of unaffected cathodic phases in the surface in case of the laser treated samples. The analogous studies using Nd-YAG lasers in N_2 and air medium by Yue *et al.* also exhibited considerable improvement in electrochemical properties due to similar mechanisms [81]. But, since irradiation power of the Nd-YAG lasers was considerably higher as compared to KrF resulted, significant improvement of melt zone thickness was observed in samples treated with Nd-YAG lasers.

The lasers that are commonly reported to be used for LSE of Al alloys are the Nd-YAG, CO_2, and excimer lasers. However, investigation of the effect of high power diode laser (HPDL) for LSM of 7075-T6 alloys (rather unconventional lasers for laser surface engineering applications) was reported by Benedetti *et al* [82]. The HPDL lasers are noted for their shorter wavelengths, reported to be as low as 405 nm. Since the power transfer efficiency increases with decreasing wavelengths, more energy per unit area can be achieved with semiconductor lasers. The LSM was performed using a HPDL laser with a power of 3.3 kW and the spot-size was defocussed to 3×3 mm. The surface temperature was controlled and varied from 720°C to 780°C by controlling laser power (close loop control). The scanning velocities were varied from 2 to 6 mm/s, and surface oxidation was prevented by using argon as a shield gas. The influence of change in surface temperature on the melt zone thickness was quantified. The experiments revealed that increasing surface temperature from 720° to 780° C increased melt zone thickness by 58%. However, decreasing the laser scanning velocity from 6 to 2 mm/s increased surface the melt-zone thickness very mildly (by about 6.4%). This behavior was inferred to be governed by the high thermal conductivity of Al, and hence, decreasing scanning velocity essentially increases time for the bulk material to get heated up instead of localized heating of the surface. Microstructural and XRD analysis of the laser treated surface revealed existence of various intermetallic phases such as $Al_{18}Mg_3Cr$, $MgZn_2$, $Mg(ZnCuAl)_2$, AlCuMg, $Fe_{24}Cu_4Al_{72}$, and Mg_2Si. The microstructures were reminiscent to cast microstructures with microsegregation inside the dendrites as detected in EDS characterization. The

second-phase particle density was observed to increase significantly along the grain boundaries due to very low solute concentration in the core. Also, existence of a unique partial melted zone was noted, wherein a part of the grains appeared to have no fusion and were an extension of the bulk material's grains. However, the region of the grains closer to the surface melt region resolidified to dendritic structures.

1.2.5.2 Laser Surface Alloying and Laser Composite Surfacing of 7075 alloys

The inherent high hardness and wear resistance are probably the reasons for the limited interest in LSA and LCS of 7075 alloys as compared to the more frequently reported LSM of 7075 alloys. However, developing LCS on 7075 alloys with *in-situ* aluminothermic was reported by Huang *et al* [83]. In the investigation, mixture of silica and metal oxides such as Fe_2O_3, CuO, Cr_2O_3, and TiO_2 was injected in the laser melt pool. The composite surfacing was performed using a CO_2 laser with spot diameter of 2 mm, scanning velocity of 25 mm/s, laser power of 1800 W and track overlapping of 50%. The presence of Al_2O_3 particles as well as intermetallic particles was reported in every LCS treated sample. The microhardness of the laser treated zone revealed similar values, independent of the metal oxide used in each LCS sample, and was in the range of $HV_{0.1}$1500-2300. Evidently, the extraordinary affinity for oxygen of Al coupled with intense heating due to laser irradiation triggers aluminothermic reactions in every sample. The nascent reduced metal subsequently reacts with the Al of the matrix to form aluminides. The high surface hardness was surmised to be contributed primarily by the hard α-Al_2O_3 and γ-Al_2O_3 particles, and the corresponding metal aluminides only slightly contributed in the overall surface hardness. The wear response showed similar responses as reported in the LSA of 2024 alloys by Xu *et* al [56]. The wear mechanism was identified to be primarily adhesive wear of the highly deformable base alloy at lower loads. However, abrasive wear dominated the wear mechanism at the higher loads due to abrasion from cracking and removal of hard Al_2O_3 particles.

1.3 Objective

The objective of our investigation was primarily to characterize and analyze the tribological and electrochemical properties of laser surface melted 7075 aluminum alloys. As discussed in the literature review, although influence of higher frequency laser irradiation on graphitic carbon coated materials has been extensively studied, the effect of low frequency higher power lasers such as CO_2 has been a relatively less investigated field. Again, the unique precipitation kinetics and its subsequent effect in the hardening of precipitation hardenable aluminum alloys have also attracted several research endeavors. Also, studies concerning the effect carbon alloyed aluminum alloys in the tribological and electrochemical properties have been primarily on bulk aluminum alloys. Thus, this lack in scientific studies on laser surface melted carbon coated precipitation hardenable aluminum alloys was our primary motivation in this investigation. Thus, this investigation was primarily an attempt to analyze and characterize the effect of carbon in laser assisted surface alloyed carbon-coated 7075 (Al-Zn-Mg-Cu) alloys in the tribological and electrochemical properties.

CHAPTER II

EXPERIMENTAL PROCEDURES

The AA7075 (Al-5.1Zn-2.1Mg-0.18Cu) was received with an initial heat treatment condition of T651 in form of plates with a thickness of 9.5 mm. The 7075 plates were sectioned using a mechanical saw to square plates with dimensions of 40 mm × 40 mm. The square plates were subsequently polished carefully with 1200 grit size SiC paper and cleaned with water and acetone to remove inorganic and organic impurities, respectively. Following this pre-preparation, the samples were sprayed with a colloidal solution of graphite nanoparticles suspended in a volatile organic liquid (Source: Slip Plate Black Ice). The thickness of graphite coating was carefully monitored and maintained to a range 40 ± 5 µm. The thickness was measured and controlled by covering a small area at the edge of the sample with a duct tape, and subsequently observing the step size between the exposed and unexposed regions with a non-contact optical 3D Nanovea profilometer (Model: PS50). The graphite coated samples were carefully dried to facilitate vaporization of the organic liquid and then clamped with the X-Y table to eliminate sliding during laser processing. The laser processing was performed by irradiating the graphite coated 7075 samples with a 1.5 kW CO_2 laser in continuous wave mode. Since the substrate AA7075 alloy is noted for its high thermal conductivity of 130W/m-K and low melting point of 477-635°C, the laser power employed in the irradiation experiments was reduced to 750 W to avoid unnecessary thermal distortions [84]. The scanning velocities employed in the tests were 15 mm/s, 20 mm/s, 25 mm/s, and 30mm/s. The stage movement was controlled by in-built x-y axis motion control feature of the stage (on

which the samples were clamped). Also, argon (Ar) as shield gas with 344 bar pressure was employed to restrict oxidation of the substrate during the experiments.

The microstructural analysis of the laser treated samples at lower magnifications was performed using a JEOL JSM-6360 SEM, while a JEOL JSM-633OF SEM was used for higher magnifications. Keller's reagent was used to etch the cross-section of the samples. The later SEM was equipped with an energy dispersive spectroscopy analyzer, which was employed in the EDS analysis for quantification and mapping of the elements. The XRD studies were performed using a Phillip Norelco (Model: PW1830) x-ray diffractometer operating with Cu-Kα radiation (λ = 1.54178 Å). The microhardness of the samples was measured using a Vickers microhardness tester (Model: Clark Instruments; CM-700AT) with 300 gf load and dwelling time of 15 s. Five similar measurements were taken at every point to get the statistical average value with corresponding positive and negative error bars. The wear tests were performed using a Nanovea tribometer (Model: MT/60) in ball-on-disk mode with 6 mm diameter Al_2O_3 balls to form 2 mm diameter wear tracks on the samples. A contact load of 5N and sliding velocity of 150 rpm was employed for each wear experiment. The wear tests were performed for 10 min, 20 min, and 30 min durations in each sample, and each test was repeated three times to ensure the repeatability of the experiments. The weight loss and coefficient of friction in each test were recorded and their average values were subsequently reported with corresponding error bars. The Raman tests were performed using a Witec alpha spectrometer with a 532 nm laser excitation source. Each Raman data was acquired at an intensity of 0.8 mW, spot size of 2μm and a 20x lens.

CHAPTER III

RESULTS AND DISCUSSION

3.1. XRD and microstructural analysis

The x-ray diffraction results of the as-received and laser treated samples are reported in Fig. 3.1. The figure illustrates that the base samples exhibited a relatively random grain texture, with (220) being the most prevalent grain orientation. However, the laser processed samples exhibited extensive texturing with (200) being the preferred orientation.

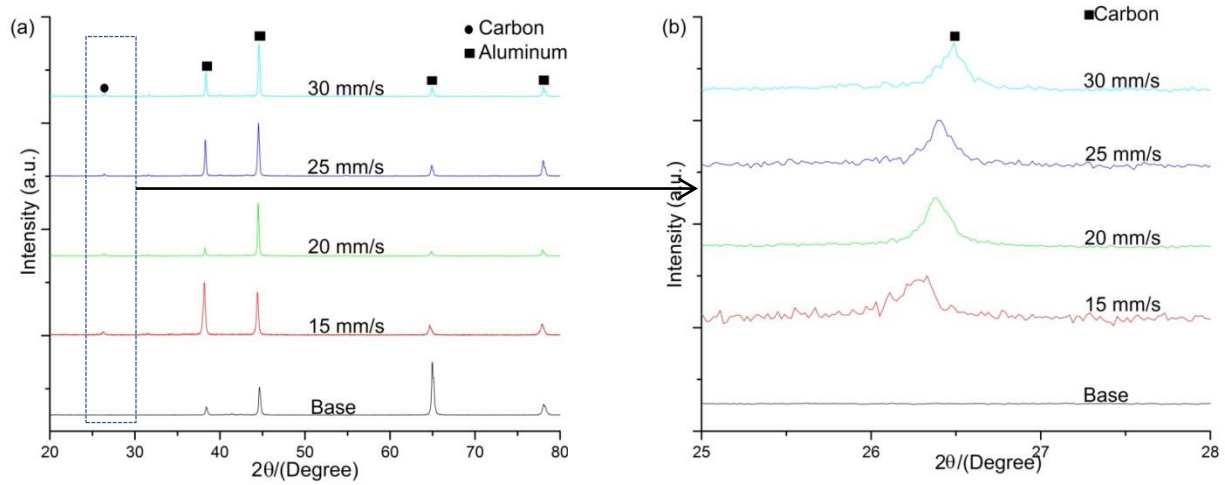

Fig. 3.1 XRD Patterns of (a) Base and Laser treated samples, and (b) Magnified XRD pattern of carbon-rich zone

It should be noted that, Al has an FCC crystal structure which do not exhibit diffraction peaks for (100) planes due to destructive interference [28]. Also, since the (100) and (200) planar systems are highly similar, consequently, preferential orientation of (200) planes essentially means a similar preferred orientation of (100) planes. Obviously, such texturing occurs primarily because the surface microstructural evolution is governed by solidification kinetics of the laser generated surface melt pool. As the surface energy of (100) planes are significantly higher than (111) and (220), the resolidification of the grains are notably higher of the (100) (and accordingly (200)) planes.

It can also be observed from the XRD plots is the presence of elemental carbon in the aluminum matrix, as observed in Fig 3.1(b) (Confirmed from ICDD database PDF no. 00-008-0415). The XRD peaks were also observed to exhibit increase in lateral shifting with increase in scanning velocity. Similar shifts in XRD patterns of LiF impact specimens were also observed by Rigg *et al.* [85], and the reason was attributed to the locked-in compressive elastic stresses. Therefore, the increase in scanning velocity increased the cooling rate, which in turn increased the thermal stresses in the material and resulted in increase in lateral shifts. Also, it that can be observed is the absence of metal carbide peaks, suggesting very low volume of carbides (if any) in the matrix that was not in the detectable range of the XRD apparatus. It is rather unusual because Al is a highly electropositive element and molten Al has been reported to often react with C to form Al_4C_3 [86]. Therefore, the lack of detectable Al_4C_3 is most likely due to the extremely high solidification rates associated with laser processing[87], which severely limits overall contact time of molten Al and C, restricting Al_4C_3 formation. This confirms that the carbon in the matrix exists in mostly elemental form instead of complex metal carbides.

The microstructure of the laser treated samples has been presented in Fig. 3.2. It can be observed that the thickness of the laser treated zone slightly increased with decrease in scanning velocities, similar to the observations reported by Benedetti *et al* [82]. It was inferred to be primarily a result of the high

thermal conductivity of Al alloys, as decreasing scanning velocity essentially conducts the thermal energy to the bulk material instead of increasing the surface temperature. The extensive heat transfer associated with continuous wave mode of laser also considerably increased surface melt-zone thickness which can be observed to be in the range of 300 – 400 μm. The significantly thicker melt-zone also ensured availability of fresh embedded carbon nano-particles for considerable period of sliding time, as carbon free unmelted matrix can be exposed only after removal of the top resolidified layer.

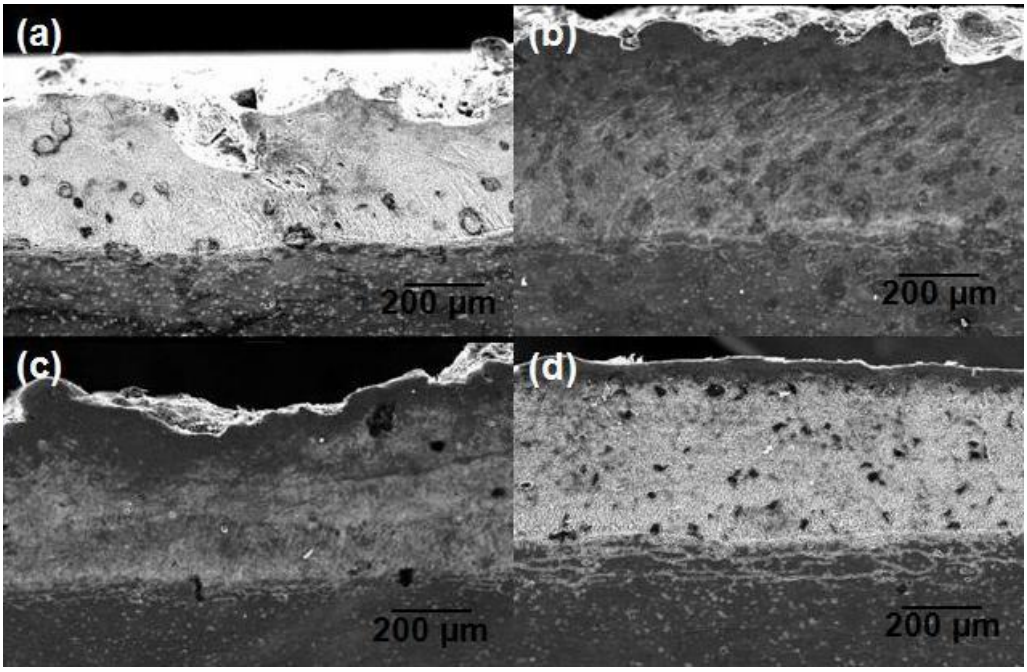

Fig. 3.2 Low Magnification microstructures of laser processed samples with following scanning velocities: (a) 15mm/s, (b) 20 mm/s, (c) 25 mm/s, and (d) 30 mm/s

3.2 Microhardness and wear behavior

The variation of microhardness with distance from the surface of the laser treated samples is presented in Fig. 3.3. It can be observed that the surface hardness decreased in the laser treated materials. This phenomenon was attributed to two major phase transformations at the vicinity of the surface. Firstly, impregnation of surface with the graphite, a rather soft material, reduces the hardness of the surface.

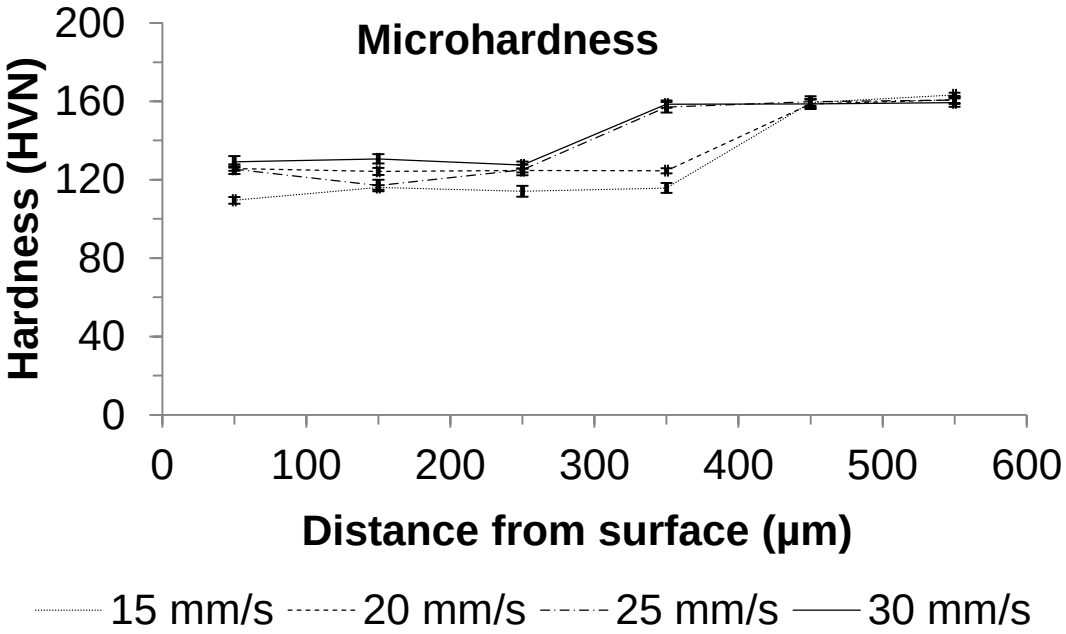

Fig. 3.3 Variation of microhardness of laser treated samples with depth from surface

Also, the high strength and hardness of the 7075 alloys are primarily a consequence of the presence of intermetallic precipitates in their microstructure. Hence, as the resolidification process post laser irradiation triggers dissolution of the precipitates, it results in a much softer surface. The hardness variation was observed to increase with increase in laser scanning velocity. It seems to occur due to the phase transformation of graphitic sp2 carbon to significantly harder DLC in the laser treated samples, as observed in the Raman spectroscopy analysis (discussed later). Hence, an increase in volume fraction of the hard DLC phase results in increase in the surface hardness. Also, since the temperature of the bulk increases with decrease in scanning velocity, it, in turn, may trigger overageing of the particles and hence reducing surface hardness.

The dry wear data is presented in Fig. 3.4. An unusual relationship was observed in the variation of wear rate with the surface hardness of the laser treated materials. Usually, the wear resistance and surface hardness is directly related and decrease in surface hardness often results in a corresponding

decrease in wear resistance. The results, however, exhibited a considerably different trend. Surface hardness was observed to decrease in the laser treated samples; however, the wear resistance was observed to increase with increase in scanning velocity. For example, while the average wear rate of the as-received materials after 30 minutes was observed to be 1.29×10^{-2} mg $N^{-1}m^{-1}$, the wear rates of 15 mm/s, 20 mm/s, 25 mm/s, and 30 mm/s laser treated samples were observed to be 1.09×10^{-2} mg $N^{-1}m^{-1}$, 0.99×10^{-2} mg $N^{-1}m^{-1}$, 0.92×10^{-2} mg $N^{-1}m^{-1}$, 0.85×10^{-2} mg $N^{-1}m^{-1}$, respectively.

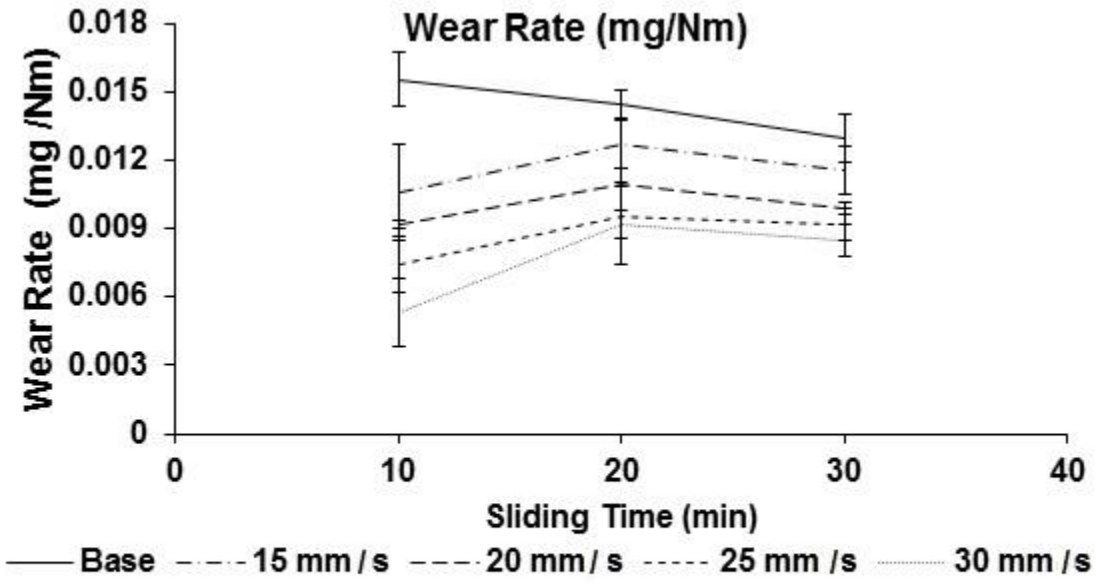

Fig. 3.4 Wear rate variation in base and laser treated samples

This unusual observation, therefore, suggested formation of a highly wear resistant tribolayer during the wear process. Hence, an extensive study to establish the wear mechanism was performed, which included analysis of coefficient of friction, wear scars, and counterbodies.

The wear mechanism was confirmed to be abrasive in nature in the SEM investigations of the wear tracks. The fissures and scratches observed in the Fig. 3.5 exhibit typical characteristics of abrasive wear, expected due to the extremely high hardness difference of the Al_2O_3 counterbodies compared to the matrix.

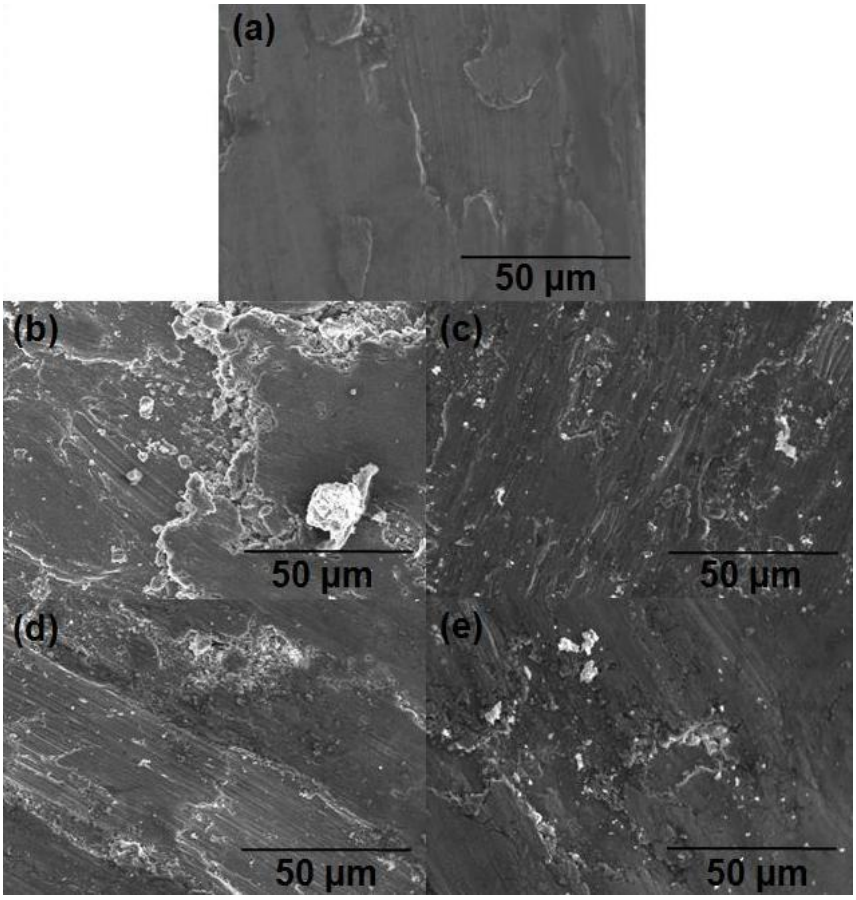

Fig. 3.5 SEM micrographs of wear scar images of (a) Base, (b) 15mm/s, (c) 20 mm/s, (d) 25 mm/s, and (e) 30 mm/s

The extent of surface damage as observed from the furrows and fissures at the surface was noted to increase in the laser treated samples, presented in Fig. 3.5(b)-3.5(e) while the base, reported in Fig. 3.5(a), exhibited minimum surface damage. Apparently, this feature contradicts the wear rate analysis which depicted improvement in wear resistance with increase in scanning velocity while SEM results suggested increase in surface damage with the same. This apparent contradictory behavior was explained in the EDS analysis of the wear tracks and the microhardness variation.

The EDS analysis, presented in Fig. 3.6, was performed for mapping of the elements and revealed extensive presence of carbon at the wear tracks. This feature, therefore, confirmed the formation of a carbon-rich tribolayer during the wear process.

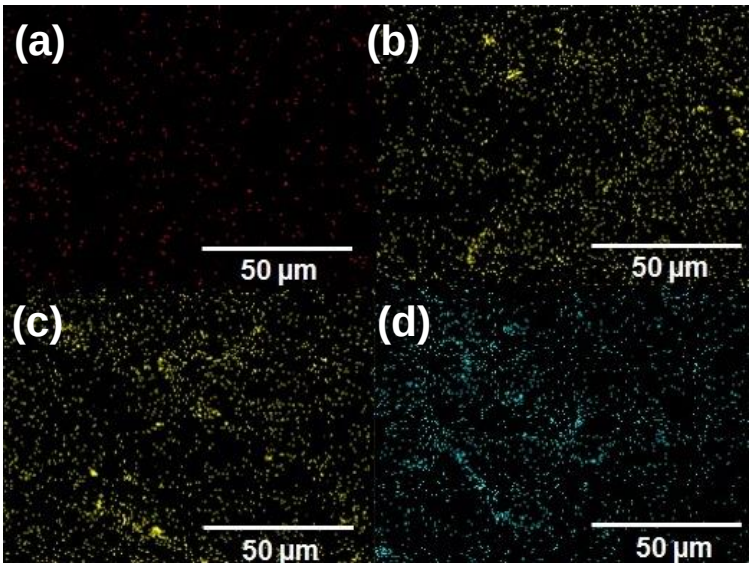

Fig. 3.6 Carbon mapping images using EDS for (a) 15 mm/s, (b) 20mm/s, (c) 25 mm/s, and (d) 30 mm/s samples

Thus, the lubricating effect of carbon-rich tribolayer was considerably high in the laser treated samples and was able to counter the aggravating effect on wear resistance in reduction of surface hardness. The coefficient of friction (COF) analysis indicated that the base exhibited an approximate COF of 0.35 in the first 10 minutes of sliding time, as observed in Fig. 3.7(a). However, the COF values of the wear bodies were considerably smaller, even though laser processing increased the surface

roughness of the materials. Also, a very interesting feature was noted in the laser processed materials in the variation of COF with sliding time. It was observed that the 15 mm/s samples exhibited an apparently stable wear mechanism, as observed from Fig. 3.7(b). However, the 20 mm/s, 25 mm/s and 30 mm/s exhibited a metastable tribolayer that transformed with time as observed from the inflection in COF after few minutes of initial wear process, as observed from Fig 3.7(c), 3.7(d), and 3.7(e) respectively. The onset time for the transformation of the tribolayer was observed to increase with increase in scanning velocity. This observation, therefore, suggests that increasing scanning velocity increased the stability of the surface, and hence, also of the tribolayer. However, this explanation contradicts the apparent stability of the 15 mm/s sample. Hence, it can be safely stated that the slow scanning velocity of 15 mm/s does not increase the stability of the surface layer; rather, it renders the surface significantly more unstable, and thus the transformation of the metastable surface layer occurs almost instantaneously and hence is undetected.

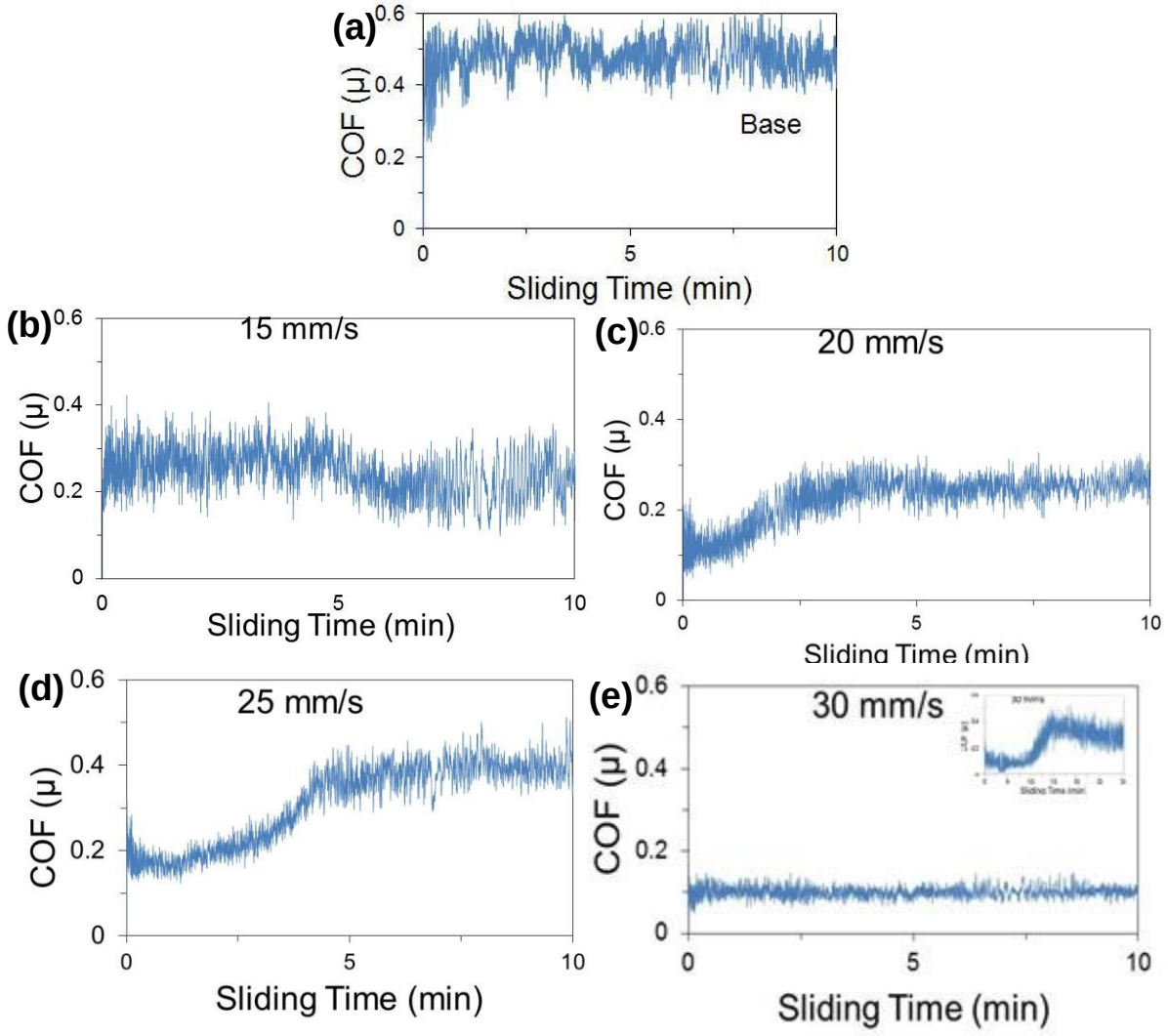

Fig. 3.7 Coefficient of friction variation with sliding time in (a) Base, (b) 15 mm/s, (c) 20 mm/s, (d) 25 mm/s, and (e) 30 mm/s laser treated samples (the transformation occurs after 10 min as shown in the subset)

Another feature that can be observed is the marginal increase in COF values with increase in time, as observed in the 30 min samples presented in Fig. 3.8(b) against the 10 min data presented in Fig.3.8 (a). Now, considering the use of non-hydrogenated graphitic sp2 nano-particles as precursor carbon and dry wear test conditions, the DLCs can be expected to be mostly non-hydrogenated. The non-hydrogenated DLCs are noted for the lack of weakly bonded hydrogen atoms, unlike the hydrogenated DLCs. Therefore, the stabilizing action of the hydrogenated DLCs is absent in the non-hydrogenated

DLCs due to the hydrogen atoms. The absence of this stabilization effect has been reported to initiate the tendency of non-hydrogenated DLCs to adhere to the wear counterbodies and thereby exacerbation of wear with increase in sliding time has been reported by Donnet *et al* [15]. Therefore, it appears that although the non-hydrogenated DLCs are not completely stable and often adhere to the counterbodies to get removed, the continuous presence of DLCs along the entire wear track mitigates this apparent removal of nano-lubricants. Hence, expensive pre-preparations like CVD [22], RF glow discharge [88] associated with hydrocarbon coatings to form hydrogenated DLCs can be avoided.

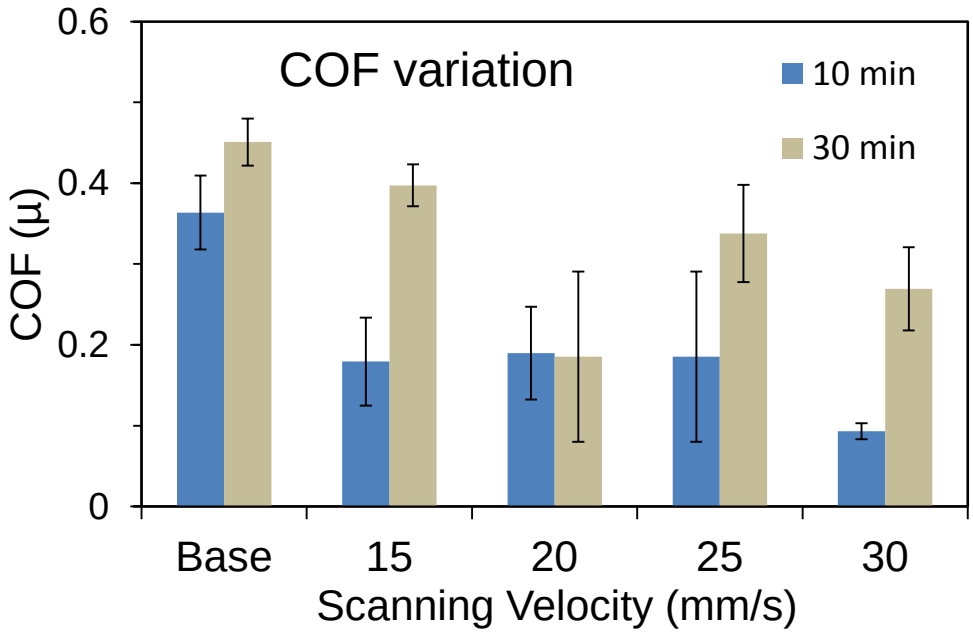

Fig. 3.8 Overall variations in coefficient of friction in 10 min and 30 min of sliding time

3.3 Raman Spectroscopy

The presence of carbon in the wear track, the unique relationship of the wear resistance with the surface hardness, the unusual coefficient of friction results, thus, repeatedly indicated marked influence of embedded carbon in the surface properties. Therefore, the physical and chemical transformations of carbon during the laser irradiation and subsequent wear experiments were investigated using confocal

Raman spectroscopy. As observed from Fig. 3.9, the input carbon was almost completely in sp2 form as noted from the sharp and intense 1574 cm^{-1} wavenumber associated with graphite (I(G)) [89]. However, laser irradiation transformed a considerable part of this sp2 carbon to DLC form, as observed in the increase in intensities of the I(D) (1337 cm^{-1}). The laser irradiated samples also exhibited significant broadening of the peaks to halo-shaped forms, suggesting extensive defect generation, inhomogeneous lattice strains and subsequent amorphization of carbon and hence, confirming the transformed phase to be amorphous DLCs. Most probably, the combined effect of extremely high temperatures at the surface and massive thermal shocks incorporated with the very high cooling rates, triggers defect generation and subsequent DLC formation. As discussed earlier, formation of DLCs from graphitic sp2 carbon due to laser irradiation has been reported in primarily higher frequency lasers that are capable of photolytic splitting of C-C bonds [90, 91]. The operating mechanism in these experiments, however, cannot be such photolytic bond splitting due to the low photonic energies of CO_2 lasers. This hypothesis also explains that the broadening of the Raman peaks observed in the materials processed with higher scanning velocities is due to increased defect density. The effect of thermal shock and temperature in DLC formation can also be observed in the increase in right shift in the Raman peaks with increase in scanning velocity from an initial wavenumber of 1574 cm^{-1} to 1589 cm^{-1}. This right shift is indicative of the presence of huge compressive stresses generated by the abnormally high cooling rates associated with laser processing, similar to the observations reported by Wang *et al* [92]. Thus, the mechanism DLC transformation can be attributed to be primarily a result of the high compressive stresses and temperatures induced from the laser processing. Interestingly, this mechanism of DLC formation is significantly similar to conventional artificial diamond manufacturing processes of introducing very high temperature and pressure in graphite.

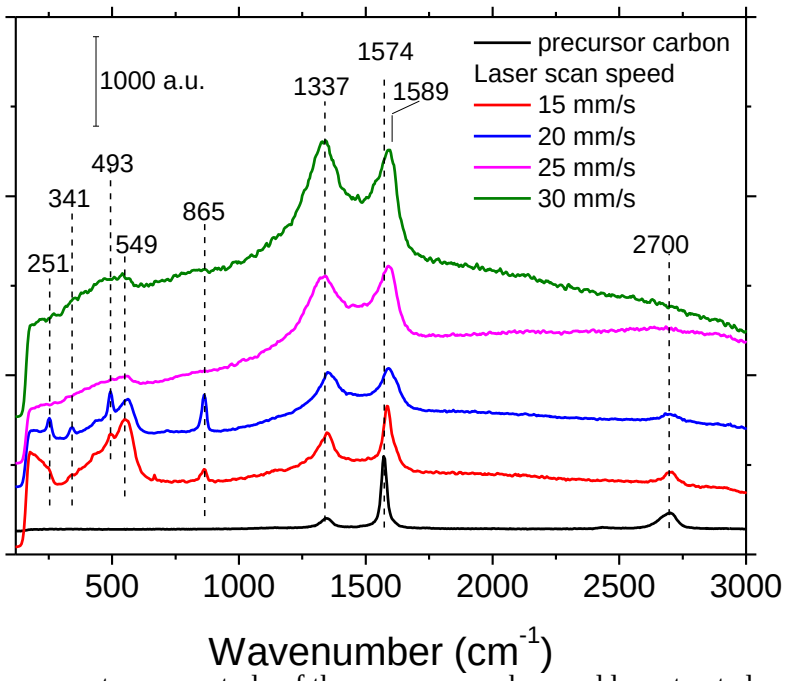

Fig. 3.9 Raman spectroscopy study of the precursor carbon and laser treated materials

The unique wear behavior of the materials was hence explained with the Raman spectroscopy investigation. The I(G) and I(D) peaks of the sample processed with 15 mm/s exhibited maximum similarity with the precursor carbon. It was also observed that increase in the scanning velocities decreases the volume of sp2 carbon while increasing the volume of DLCs. This suggests that the slower scanning velocities introduce extensive heat in the bulk, and it re-transforms the DLCs to sp2 carbon, rather similar to overageing of precipitates at lower scanning velocities. The presence of metal carbides like Al_4C_3 in the 15 mm/s and 20 mm/s samples was observed, as detected from the peak at 865cm^{-1} [93], while their presence was considerably diminished at the higher scanning velocities. Thus, this reveals that the carbon in the matrix undergoes several competing physical and chemical transformations; thus, the kinetics of re-transformation of DLCs to sp2 carbon is more dominant than the formation of metal carbides. Hence, carbide formation dominates only after a considerable amount of DLCs to sp2 carbon re-transformation is completed.

The Raman spectroscopy was also used in characterization of the wear counterbodies. Raman spectroscopy on the wear counterbodies is presented in Fig. 3.10. It can be observed that the counterbodies of all the four scanning velocities exhibited similar trends in Raman spectroscopy. This result confirms the metastable tribolayer hypothesis that was previously discussed. It appears that the carbon at the surface undergoes transformations in each of the four laser treated samples and eventually stabilizes in a particular phase mixture of DLC and sp2 carbon. Since, both DLCs [94] and sp2 carbon [95] have been reported to exhibit very low COF values; it was naturally reflected in the wear studies. However, it appears that as DLCs exhibit very high hardness unlike sp2 carbon, the contribution of DLCs in reducing wear rate is significantly higher than that of the sp2 carbon.

Another feature that can be observed is the increase in presence of DLCs in the 15 mm/s counterbody as compared to the original sample. This feature is very unique, because although shear transformation of DLCs to more stable sp2 carbon during wear has been extensively reported [96-98], the transformation of graphitic sp2 carbon to DLCs in wear has not been widely observed. However, Kirichenko *et al.* have reported the transformation of sp2 carbon onions to DLCs at shear stresses exceeding 43 GPa [99]. Obviously, generation of a stress greater than 43 GPa by a 5N load appears highly unlikely. However, it seems that the dimensions of the nanostructured carbon particles cause a load distribution such that it generates microscopic local stresses that exceed this value. Again, the 'usual' shear transformation of DLCs to sp2 carbon can also be observed in the counterbodies of the samples irradiated with higher scanning velocities like 30 mm/s. Therefore, this suggests that the evolution of the tribolayer is primarily controlled by the local shear stresses experienced by the carbon particles and their initial physical form. Also, the similar Raman spectroscopy of each counterbody infers to stabilization of the metastable tribolayer consisting of both sp2 and DLC nanoparticles.

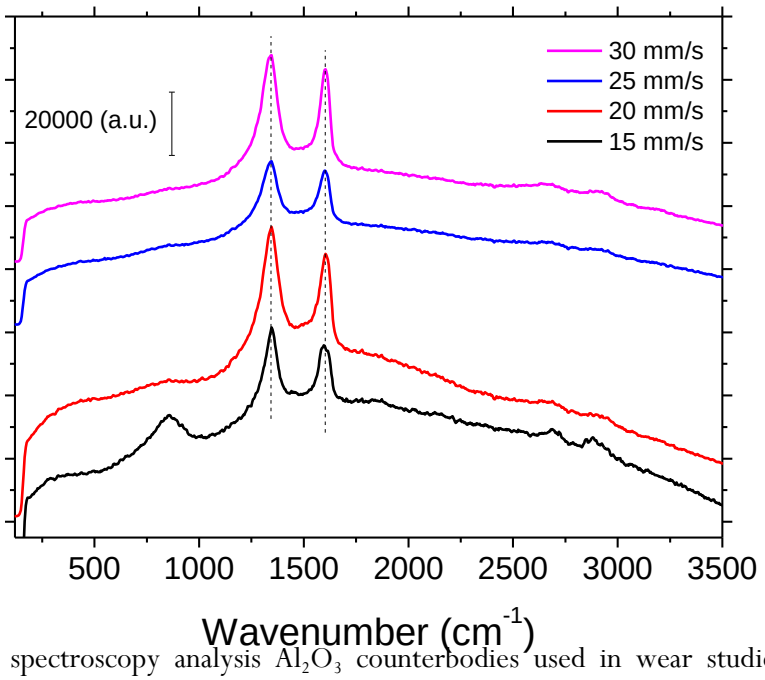

Fig. 3.10 Raman spectroscopy analysis Al_2O_3 counterbodies used in wear studies of laser irradiated samples

3.4 Electrochemical Characterization

The electrochemical characterization studies were performed by generating the Tafel plots of the base and laser treated materials, presented in Fig. 3.11. The corresponding Icorr and Ecorr can be observed in Fig. 3.12. It was revealed that the corrosion current (Icorr) in carbon coated materials increased as compared to the base. However, the corrosion potential (Ecorr) exhibited marginal improvement, suggesting that the carbon coating mildly increased the electronegativity (nobility) of the laser treated materials. The apparent increase in corrosion current suggests that laser treatment should deteriorate the corrosion resistance of the material. It should be considered, however, that the major concern with 7075 alloys has been their poor response to stress-corrosion cracking, rather than their overall corrosion rate.

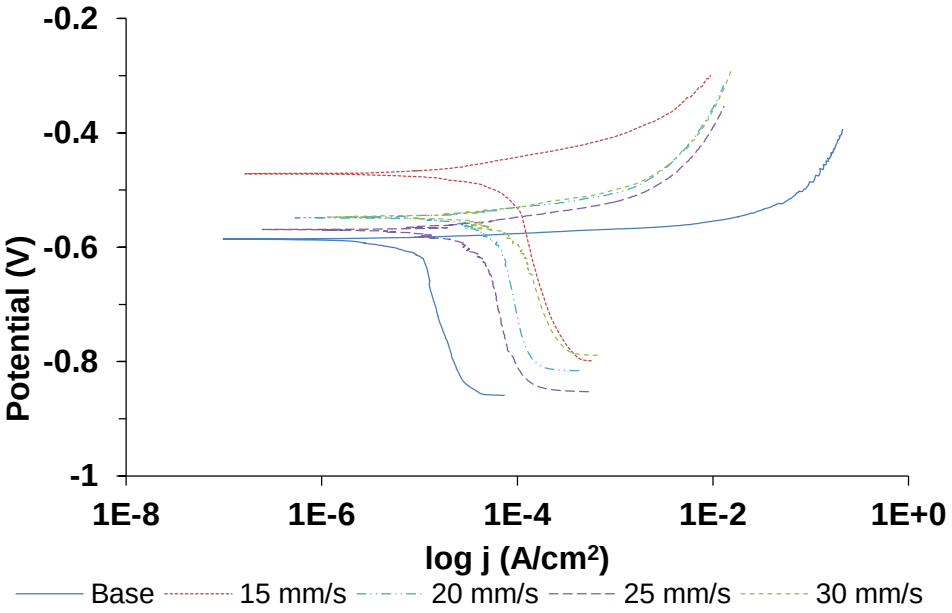

Fig. 3.11 Tafel plots of the base and laser irradiated samples

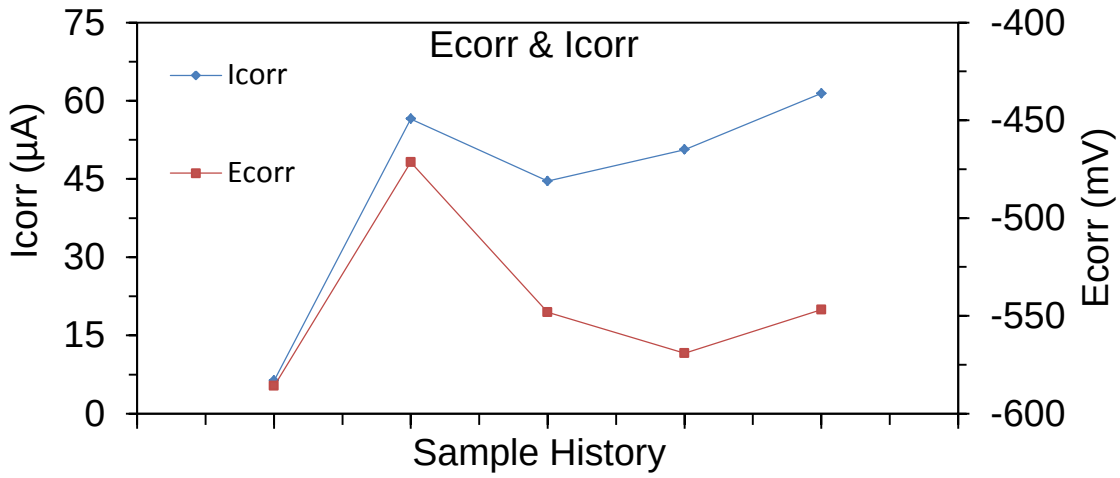

Fig. 3.12 Ecorr and Icorr of the base and laser irradiated samples

The primary reason for such low SCC values has been attributed to their tendency to pit in aggressive environments. Therefore, SEM analysis on corroded surfaces was performed to investigate the magnitude of pitting in the base and laser treated samples. It appears from Fig. 3.13(a), that the surface of the base material shows extensive pitting, a feature highly undesired in as they act as in-situ crack nucleation sites. However, the corroded surface of the laser treated

sample, as observed from Fig. 3.13(b)-3.13(e) exhibited considerably higher uniform corrosion, which can significantly reduce the SCC susceptibility of the material.

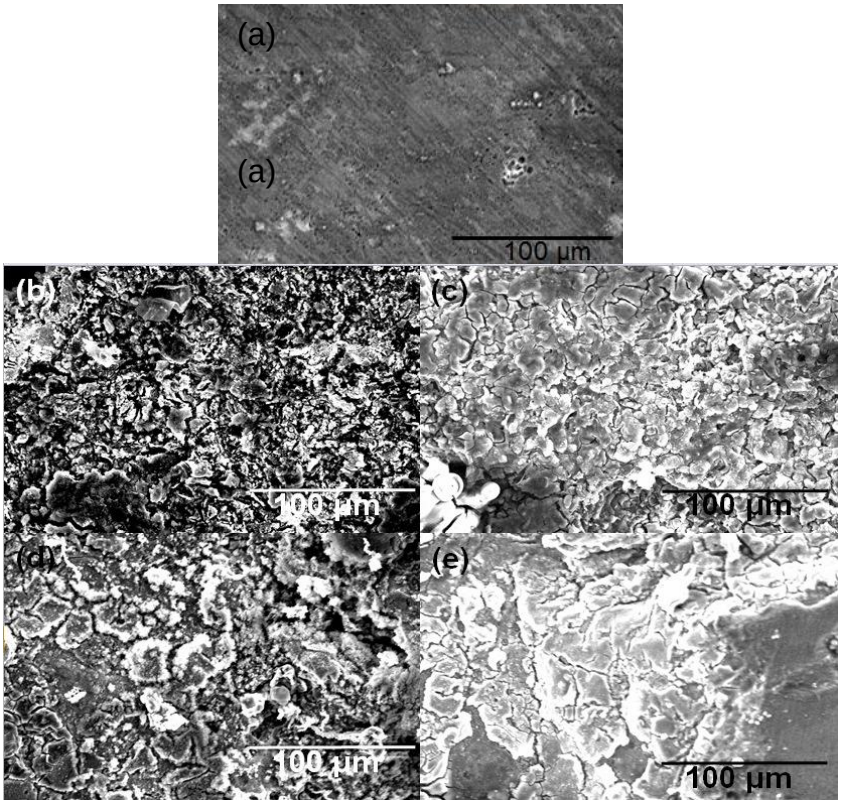

Fig. 3.13 SEM Micrographs of corroded areas of (a) Base, (b) 15 mm/s, (c) 20 mm/s, (d) 25 mm/s, and (e) 30 mm/s samples

One more feature in the electrochemical characterization should be noted here. The onset of anodic polarization in the base material occurs from a current density in the order of 10^{-1} A/cm^2. However, the anodic polarization in the laser treated samples commenced at a current density value less than almost an order of magnitude of the base. This unique response in corrosion of the material can again be associated with the presence of carbon in the laser treated zone. Since both DLCs and sp2 carbon are highly electronegative materials, these particles operate primarily as impregnated cathodes in surface of the materials, as compared to the base material, wherein the intermetallic precipitates acts as the primary cathodic sites. Therefore, the finely distributed carbon particles trigger a highly uniform corrosion

mechanism; consequently, superior and more conformal corrosion film was generated in the laser treated materials. However, as corrosion in the base material was localized primarily around the vicinity of the electronegative precipitates, extensive pitting was observed. This observation can also be extrapolated in another very crucial conclusion. Since the 7075 alloys are one of the most popular industrial materials and therefore, are often used with other dissimilar materials. Thus, its use with other dissimilar materials generates a strong probability of formation of a galvanic couple and thereby initiation of galvanic corrosion with the corresponding dissimilar material. Thus, an increase in the value of Ecorr as well as onset of anodic passivation at lower corrosion current density can be highly critical parameters in improving its galvanic corrosion behavior. This is because an increase in Ecorr essentially means increase in electronegativity and therefore increases its chances to form cathode. Also if a 7075 alloy is connected with a nobler material to form the anode in a galvanic couple, passivation of the laser treated material would begin significantly earlier (approximately at a corrosion current density less than one-tenth of the base material). This also underlines the importance of laser treatment in improving the galvanic corrosion resistance of the materials.

CHAPTER IV

CONCLUSION

The CO_2 laser was successfully employed to develop nano-carbon embedded coatings in AA7075-T651 alloys in continuous wave mode. The wear analysis confirmed the mechanism to be primarily abrasive in nature, with the abrasive nature getting aggravated by the softened surfaces of the laser processed samples. This softening was due to the dissolution of precipitates in the laser treated zones. The wear resistance increased with increase in scanning velocities due to the lubricating action of the embedded graphitic and DLC nanoparticles. The DLC to sp2 carbon ratio increased with increase in scanning velocities due to reduction in accumulated thermal energy, limiting the retransformation of DLCs and defect-populated sp2 carbon to defect-free sp2 carbon. The presence of the metastable DLCs in higher scanning velocity processed samples improved wear resistance due to their inherent high hardness and low friction properties. The tribological studies also indicated ‘two-way’ phase transformations of the carbon particles, wherein both DLC to sp2 (higher scanning velocities) and sp2 to DLC (lower scanning velocities) were detected. It was attributed to the spatial relaxation and abnormal stress distribution effects, respectively. The electrochemical characterization indicated notable improvement in pitting behavior and galvanic corrosion in the carbon-coated samples.

REFERENCES

[1] D. Berman, A. Erdemir, A.V. Sumant, Carbon, 54 (2013) 454-459.

[2] E.J. Sandoz-Rosado, O.A. Tertuliano, E.J. Terrell, Carbon, 50 (2012) 4078-4084.

[3] S. Suárez, A. Rosenkranz, C. Gachot, F. Mücklich, Carbon, 66 (2014) 164-171.

[4] A.A. Al-Azizi, O. Eryilmaz, A. Erdemir, S.H. Kim, Carbon, 73 (2014) 403-412.

[5] R.H. Savage, Journal of Applied Physics, 19 (1948) 1-10.

[6] A. Voevodin, M. Donley, J. Zabinski, Surface and Coatings Technology, 92 (1997) 42-49.

[7] Y. Yamagata, A. Sharma, J. Narayan, R.M. Mayo, J.W. Newman, K. Ebihara, Journal of Applied Physics, 86 (1999) 4154-4159.

[8] M. Hakovirta, X.M. He, M. Nastasi, Journal of Applied Physics, 88 (2000) 1456-1459.

[9] X.L. Peng, Z.H. Barber, T.W. Clyne, Surface and Coatings Technology, 138 (2001) 23-32.

[10] V. Yadav, S.P. Harimkar, Advanced Engineering Materials, 13 (2011) 1128-1134.

[11] W. Ma, J. Lu, Wear, 270 (2011) 218-229.

[12] T. Borkar, S. Harimkar, Surface Engineering, 27 (2011) 524-530.

[13] V. Batusov, J. Budagov, V. Flyagin, J. Khubua, Y. Lomakin, M. Lyablin, N. Rusakovich, D. Schabalin, N. Topilin, M. Nessi, Part. Nucl. Lett, 102 (2001) 33-40.

[14] Y. Chen, Y.-W. Chung, S.-Y. Li, Surface and Coatings Technology, 200 (2006) 4072-4077.

[15] C. Donnet, J. Fontaine, A. Grill, T. Le Mogne, Tribology Letters, 9 (2001) 137-142.

[16] J.D. Schall, G. Gao, J.A. Harrison, The Journal of Physical Chemistry C, 114 (2009) 5321-5330.

[17] H.-J. Scheibe, B. Schultrich, Thin Solid Films, 246 (1994) 92-102.

[18] A. Voevodin, A. Phelps, J. Zabinski, M. Donley, Diamond and Related Materials, 5 (1996) 1264-1269.

[19] A. Voevodin, J. Jones, T. Back, J. Zabinski, V. Strel'nitzki, I. Aksenov, Surface and Coatings Technology, 197 (2005) 116-125.

[20] M. Jelínek, K. Smetana, T. Kocourek, B. Dvořánková, J. Zemek, J. Remsa, T. Luxbacher, Materials Science and Engineering: B, 169 (2010) 89-93.

[21] N.B. Dahotre, S. Harimkar, Laser Fabrication and Machining of Materials, Springer, 2008.

[22] P.R. Buerki, S. Leutwyler, Journal of Applied Physics, 69 (1991) 3739-3744.

[23] M. Baydoğan, H. Çimenoğlu, E. Sabri Kayalı, Wear, 257 (2004) 852-861.

[24] B. Venkataraman, G. Sundararajan, Wear, 245 (2000) 22-38.

[25] J.L. Mo, M.H. Zhu, J.F. Zheng, J. Luo, Z.R. Zhou, Tribology International, 43 (2010) 912-917.

[26] M.H. Zhu, Z.R. Zhou, Wear, 255 (2003) 269-275.

[27] T.M. Yue, C.F. Dong, L.J. Yan, H.C. Man, Materials Letters, 58 (2004) 630-635.

[28] https://www.alcoa.com/global/en/about_alcoa/pdf/Smeltingpaper.pdf

[29] http://www.worldofwallstreet.us/metals-annual-production-.html

[30] http://www.ceicdata.com/en/press/ceic-newslert-us-geological-survey-non-ferrous-metals-production-statistics

[31] K.R. Van Horn, Aluminium. Vol. 1, American Society for Metals, Metals Park, 1967.

[32] M. Pohl, O. Storz, T. Glogowski, Materials Characterization, 58 (2007) 65-71.

[33] S. Serajzadeh, H. Sheikh, Materials Science and Engineering: A, 486 (2008) 138-145.

[34] J. Chipman, MT, 3 (1972) 55-64.

[35] I.J. Polmear, Light alloys : metallurgy of the light metals, Halsted Press, New York ; Toronto, 1996.

[36] C. Blanc, S. Gastaud, G. Mankowski Journal of The Electrochemical Society, 150 (2003) B396-B404.

[37] R.E. Pawel, G.L. Yoder, D.K. Felde, B.H. Montgomery, M.T. McFee, Oxidation of Metals, 36 (1991) 175-194.

[38] T. Minoda, H. Yoshida, Metall and Mat Trans A, 33 (2002) 2891-2898.

[39] International Journal of Corrosion, 2012 (2012).

[40] B. Mazurkiewicz, A. Piotrowski, Corrosion Science, 23 (1983) 697-707.

[41] L.A.B. Mabhali, N. Sacks, S. Pityana, Wear, 290–291 (2012) 1-9.

[42] J.H. Abboud, D.R.F. West, J Mater Sci Lett, 9 (1990) 308-310.

[43] M.B. Lekala, J.W. van der Merwe, S.L. Pityana, International Journal of Corrosion, 2012 (2012) 4.

[44] C.M. Liao, J.M. Olive, M. Gao, R.P. Wei, Corrosion, 54 (1998) 451-458.

[45] C. Augustin, E. Andrieu, C. Blanc, G. Mankowski, J. Delfosse, Journal of The Electrochemical Society, 154 (2007) C637-C644.

[46] M. Keddam, C. Kuntz, H. Takenouti, D. Schustert, D. Zuili, Electrochimica Acta, 42 (1997) 87-97.

[47] R. Li, M.G.S. Ferreira, A. Almeida, R. Vilar, K.G. Watkins, M.A. McMahon, W.M. Steen, Surface and Coatings Technology, 81 (1996) 290-296.

[48] Z. Liu, P.H. Chong, A.N. Butt, P. Skeldon, G.E. Thompson, Applied Surface Science, 247 (2005) 294-299.

[49] Z. Liu, P.H. Chong, P. Skeldon, P.A. Hilton, J.T. Spencer, B. Quayle, Surface and Coatings Technology, 200 (2006) 5514-5525.

[50] M. Zimmermann, M. Carrard, W. Kurz, Acta Metallurgica, 37 (1989) 3305-3313.

[51] M.A. Sutton, B. Yang, A.P. Reynolds, R. Taylor, Materials Science and Engineering: A, 323 (2002) 160-166.

[52] M.A. Sutton, B. Yang, A.P. Reynolds, J. Yan, Materials Science and Engineering: A, 364 (2004) 66-74.

[53] P. Kadolkar, N.B. Dahotre, Applied Surface Science, 199 (2002) 222-233.

[54] H.C. Man, C.T. Kwok, T.M. Yue, Surface and Coatings Technology, 132 (2000) 11-20.

[55] N.N.M.G.D.B. Eustathopoulos, Pergamon, Amsterdam; New York, 1999.

[56] J. Xu, W. Liu, Wear, 260 (2006) 486-492.

[57] K.-R.A.C.o.A. Van Horn, Aluminum. Vol. 2, American Society for Metals, Metals Park (Ohio), 1967.

[58] A.S.M.I. American Society for Metals, ASM International, Materials Park, OH, 1982.

[59] J.L. Murray, A.J. McAlister, Bulletin of Alloy Phase Diagrams, 5 (1984) 74-84.

[60] J. Murray, Bulletin of Alloy Phase Diagrams, 3 (1982) 60-74.

[61] L.S. Weinman, C. Kim, T.R. Tucker, E.A. Metzbower, Appl. Opt., 17 (1978) 906-910.

[62] P. Delogu, S. Tosto, Materials Letters, 20 (1994) 11-17.

[63] H.C. Man, S. Zhang, F.T. Cheng, Materials Letters, 61 (2007) 4058-4061.

[64] Y.S.D.D.P. Touloukian, Thermal radiative properties: metallic elements and alloys, IFI/Plenum, New York, 1970.

[65] S. Nayak, L. Riester, H.M. Meyer, N.B. Dahotre, Journal of Materials Research, 18 (2003) 833-839.

[66] S. Nayak, H. Wang, E.A. Kenik, I.M. Anderson, N.B. Dahotre, Materials Science and Engineering: A, 390 (2005) 404-413.

[67] Y. Fu, A.W. Batchelor, Y. Gu, K.A. Khor, H. Xing, Surface and Coatings Technology, 99 (1998) 287-294.

[68] Y. Fu, A.W. Batchelor, Surface and Coatings Technology, 102 (1998) 119-126.

[69] T. Helander, O. Tolochko, JPE, 20 (1999) 57-60.

[70] A.M. Venezia, C.M. Loxton, Surface and Interface Analysis, 11 (1988) 287-290.

[71] Y.-C. Chuang, S.-C. Lee, H.-C. Lin, MATERIALS TRANSACTIONS, 47 (2006) 1140-1144.

[72] L.R. Katipelli, A. Agarwal, N.B. Dahotre, Applied Surface Science, 153 (2000) 65-78.

[73] M.I. Pech-Canul, R.N. Katz, M.M. Makhlouf, S. Pickard, Journal of Materials Science, 35 (2000) 2167-2173.

[74] H.C. Man, Y.Q. Yang, W.B. Lee, Surface and Coatings Technology, 185 (2004) 74-80.

[75] P.H. Chong, H.C. Man, T.M. Yue, Surface and Coatings Technology, 145 (2001) 51-59.

[76] J. Santner, MTA, 9 (1978) 769-779.

[77] C.P. Chan, T.M. Yue, H.C. Man, Journal of Materials Science, 38 (2003) 2689-2702.

[78] I.J. Polmear, M.J. Couper, MTA, 19 (1988) 1027-1035.

[79] S. Maitra, G.C. English, MTA, 12 (1981) 535-541.

[80] B. Sarkar, M. Marek, E.A. Starke, MTA, 12 (1981) 1939-1943.

[81] T.M. Yue, L.J. Yan, C.P. Chan, Applied Surface Science, 252 (2006) 5026-5034.

[82] A. Benedetti, M. Cabeza, G. Castro, I. Feijoo, R. Mosquera, P. Merino, Surface and Interface Analysis, 44 (2012) 977-981.

[83] X.L. Kaijin HUANG, Changsheng XIE, T.M.Yue, J. Mater. Sci. Technol., 23 (2007) 201-206.

[84] A.A.S.M. Inc.

[85] P.A. Rigg, Y.M. Gupta, Applied Physics Letters, 73 (1998) 1655-1657.

[86] M.F. Amateau, Journal of Composite Materials, 10 (1976) 279-296.

[87] A. Singh, S. Harimkar, JOM, 64 (2012) 716-733.

[88] N.I. Chapliev, T.V. Kononenko, A.A. Smolin, V.E. Strelnitsky, Surface and Coatings Technology, 47 (1991) 730-739.

[89] F. Tuinstra, J.L. Koenig, The Journal of Chemical Physics, 53 (1970) 1126-1130.

[90] F. Bourquard, T. Tite, A.-S. Loir, C. Donnet, F. Garrelie, The Journal of Physical Chemistry C, 118 (2014) 4377-4385.

[91] Á. Mechler, P. Heszler, Z. Kántor, T. Szörényi, Z. Bor, Applied Physics A, 66 (1998) 659-661.

[92] W. Yuejian, E.P. Joseph, K. Boris, K.M.L. Kanani, Scientific Reports, 2 (2012).

[93] R. Pérez Bustamante, M. Miki Yoshida, R. Martínez Sánchez, J. Bonilla Martinez, J. González Cantu, Microscopy and Microanalysis, 18 (2012) 1914-1915.

[94] M. Kalin, I. Velkavrh, J. Vižintin, L. Ožbolt, Meccanica, 43 (2008) 623-637.

[95] T. Filleter, J.L. McChesney, A. Bostwick, E. Rotenberg, K.V. Emtsev, T. Seyller, K. Horn, R. Bennewitz, Physical Review Letters, 102 (2009) 086102.

[96] Y.A.N. Liu, E.I. Meletis, Journal of Materials Science, 32 (1997) 3491-3495.

[97] Y. Liu, A. Erdemir, E.I. Meletis, Surface and Coatings Technology, 86–87, Part 2 (1996) 564-568.

[98] T.-B. Ma, Y.-Z. Hu, H. Wang, Carbon, 47 (2009) 1953-1957.

[99] A.N. Kirichenko, A.K. Aseev, V.N. Denisov, I. Perezhogin, B.A. Kulnitskiy, A.A. Nuzhdin, V.D. Blank, MRS Online Proceedings Library, 1452 (2012).

VITA

Sourabh Biswas

Candidate for the Degree of

Master of Science

Thesis: LASER SURFACE MELTING OF CARBON COATED AA7075 ALUMINUM ALLOY: STRUCTURAL TRANSFORMATIONS AND TRIBOLOGICAL BEHAVIOR

Major Field: Mechanical and Aerospace Engineering

Biographical:

Education:

Completed the requirements for the Master of Science/Arts in Mechanical and Aerospace Engineering at Oklahoma State University, Stillwater, Oklahoma July, 2014. GPA: 3.5 (of 4)

Completed the requirements for the Bachelor of Engineering in Metallurgy and Materials Engineering at Bengal Engineering and Science University, Shibpur, West Bengal, India in July 2011. GPA: 8.98 (of 10)

Experience:

Graduate Research Assistant (Multiscale Materials Processing and characterization):

- Successfully performed laser processing of metallic and ceramic materials using high power CO_2 laser.
- Highly trained in electrochemical (corrosion) and tribological (wear) characterization of engineering materials.
- Extensively performed x-ray diffraction (XRD), scanning electron microscopy (SEM), and energy dispersive spectroscopy (EDS), Raman spectroscopy for characterization of research samples.

Graduate Teaching Assistant (Lead TA for senior level MAE4333 for Fall 12, 13 and Spring 13 and 14):

- Delivered lectures concerning theories of mechanical metallurgy.
- Performed and assisted students in heat treatment of Steel, Aluminum and Amorphous Metallic Alloys
- Extensive experience in mechanical characterization of materials, such as, fatigue, impact, tensile, and microhardness testing of materials.